

# High resolution atomic scale characterization of dislocations in high entropy alloys: Critical assessment of template matching and geometric phase analysis

F. Brenne<sup>1</sup>, A.S.K. Mohammed<sup>1</sup>, H. Sehitoglu<sup>\*</sup>

University of Illinois at Urbana-Champaign, Department of Mechanical Science and Engineering, 1206 W Green St, Urbana, Illinois, 61801, USA

## ARTICLE INFO

### Keywords:

Scanning transmission electron microscopy  
Displacement analysis  
Template matching  
Geometrical phase analysis  
High entropy alloy

## ABSTRACT

The paper assesses the applicability of advanced atomic resolution displacement measurement techniques to characterize dislocation character in metallic materials using simulated images derived from anisotropic elasticity and actual measurements in high entropy alloys. We draw attention to two techniques: the real space method of template matching (TeMA) and the reciprocal space method of geometric phase analysis (GPA) and provide a critical assessment. These techniques have limitations for direct evaluation of full dislocations Burgers vector or when local displacements are exceeding 50% lattice spacing. This is clearly illustrated with simulated arctangent displacement profiles reminiscent of dislocation cores. An approach for circumventing this limitation is suggested in the form of a nearest neighbor correction. Additionally, a methodology for determination of the Burgers vector is introduced on the basis of a vectorial rendering of the displacement field upon consideration of two zone axis measurements and applied to TeMA and GPA. The experimental results conform to the Burgers vector of a full lattice dislocation in the FCC crystal structure of the High-Entropy Alloy (HEA). The comparison of simulated and experimental images proves the efficacy of the HR-TEM (High Resolution Transmission Electron Microscopy) displacement mapping techniques while pointing to the need for caution in case of large displacements.

## 1. Introduction

### 1.1. Importance and methods for atomistic displacement and strain determination

For a large variety of materials the defect structure is of pivotal role for the part performance in practice. In metals for structural applications for example, the density and mobility of dislocations is of utmost importance for the resistance against plastic deformation and the damage evolution behavior under static and cyclic loading conditions [1, 2]. In more advanced alloys, such as shape memory alloys, the arrangement of dislocations at phase interfaces governs the reversibility of the phase transformation and, thus, the stability of the functional part performance [3, 4]. Finally, the increased strains arising from dislocations at interfaces are known to enhance the mobility of charge carriers in semiconductors [5, 6].

A theoretical model for a quantitative description of stress levels for

motion of crystal dislocations was developed by Peierls [7] and extended by Nabarro [8] and Foreman [9]. However, as the distortions induced by dislocations is limited to an area of several atoms only, transmission electron microscopy needs to be employed for direct observation of dislocations and it was not until the more recent development of high resolution transmission electron microscopy (HRTEM) that these phenomena could be experimentally quantified [10].

Due to the highly repetitive pattern of the atomic lattice in the recorded images and the presence of very small displacements only, straightforward evaluation of the displacement and strain fields around defects is not possible, which is why digital image processing techniques need to be employed [11]. Earlier established methods, such as digital image correlation, are not applicable as these rely on identification of individual sample areas having a stochastic intensity distribution and tracking these areas in the course of elastoplastic deformation [12–14]. Their applicability is restricted to scales of continuum deformation, seldom reaching the sub-micron regime. For examinations of

<sup>\*</sup> Corresponding author.

E-mail address: [huseyin@illinois.edu](mailto:huseyin@illinois.edu) (H. Sehitoglu).

<sup>1</sup> Both authors contributed equally to this paper.

displacements and elastic strains on atomic scale, other methods were developed, which basically can be classified into real space and Fourier space approaches.

Typical representatives of real space methods are the peak finding (PF) techniques [11, 15–21], where a two-dimensional, undistorted reference lattice is superimposed onto the recorded, two-dimensional projection of the strained crystal. It has to be noted, that the projection needs to be obtained at sufficient resolution with the incident beam being parallel to a zone axis, so that columns of atoms appear as individual dots of several pixels in the image plane. The center of these dots can then be located with sub-pixel accuracy by the maximum of their intensity distribution. The local displacements are obtained by calculating the deviations between the individual intensity maxima and the corresponding reference lattice positions. The gradients of displacements eventually provide the corresponding strain fields.

A prominent Fourier space approach is the geometric phase analysis (GPA) methodology developed by Hýtch [22] and vastly examined and applied in several follow-up studies, e.g. [23–28]. For GPA, the real space image is obtained under the same conditions as in case of PF techniques. By transformation into Fourier space the frequency distribution is revealed in form of individual Bragg spots (analogous to the reciprocal crystal lattice appearing in the diffraction plane in conventional TEM). In an ideal, perfectly regular crystal the individual lattice planes are represented by sharp diffraction spots. However, in a deformed crystal the frequency distribution is not regular and Bragg spots show deviations from their ideal position. By filtering out the information of an individual Bragg spot and retransformation into real space, the phase component of the resulting complex image provides the local shift of the corresponding lattice plane, i.e. a displacement relative to its regular position in the unstrained state. By using the information of two, non-collinear Bragg spots the two-dimensional displacement field is obtained. As in case of PF, the strain field is finally calculated by gradients of the displacements.

A similar approach as in case of GPA is followed by the more recently developed 4D scanning transmission electron microscopy (4D-STEM) techniques. These are based on combining the 2D real space ( $x, y$ ) information obtained from, e.g., the high-angle annular dark-field (HAADF) detector with the local diffraction pattern in reciprocal space ( $k_x, k_y$ ), hence the term 4D-STEM. As a highly convergent beam is used, the information is limited to the actual probe position allowing for analysis of local diffraction data. Following this approach, the local strains are obtained by analysis of the positions of individual Bragg spots (or discs in case of convergent beams) at each position of the probe [29–36]. One of the strengths of this approach is high-throughput mapping capability [30] allowing strain/orientation-mapping from the nanoscale to the meso-scale [29, 35, 37]. However, as the probe diameter is limited to about 1 nm to 2 nm [29, 37] and diffraction requires information of several atoms, analysis of individual atomic positions is not possible. Thus, displacement and strain field analysis of individual dislocations is impeded, which is why more local methods, i.e. PF and GPA, are in focus of the current study.

Practical studies using both approaches were conducted on thin films [15, 16, 22] and a large variety of semiconductors [11, 17, 22, 24, 26–28, 38, 39]. Only few works reported on minerals [40] or metals [41]. The phenomena investigated comprised, for example, the interface structure within semiconductors and related changes in lattice parameters [15, 16, 23] as well as the characteristics of different types of dislocations and their network along phase boundaries [11, 22, 24, 28, 41]. Presuming proper microscope alignment and specimen conditions, the authors found high accuracies, e.g. from 0.8% to 0.4% of the lattice constants in [16, 22] or from 0.1 Å to 0.03 Å in [15, 24], and good accordance to values obtained from theoretical models [41], atomistic simulations [28] and finite elements analysis [27]. While the advantages of PF are rooted in lower requirements with respect to CPU and memory, GPA is performing better in the presence of sublattices, when the peak positions are harder to determine by PF, which is why they are seen to be

complementary tools for accurate determination of displacement and strain fields around different types of defects at atomistic scales [17].

### 1.2. Restrictions and errors

Although displacements and strains on atomistic scale can in principle be determined with high accuracy, the reliability of the PF and Fourier space techniques is subject to certain constraints. For example, both methods are susceptible to variations in image contrast and are consequently highly influenced by defocus, local specimen thickness and changes in composition. Also, the signal-to-noise ratio plays a pivotal role, as it determines the accuracy of the peak center determination in PF as well as the frequency components used in GPA. Thus, preferably thin specimen are desired, leading in turn to difficulties with respect to thin foil relaxation, specimen warpage and/or thickness uniformity [11, 17, 22]. Hýtch and Houdellier [26], for instance, used GPA for measuring the strains within a SiGe layer and found values being clearly lower than those obtained from elastic calculations. As an optimal aberration corrected system was used, the deviation was related to relaxation of stresses in course of thin-foil preparation.

In order to overcome the necessity for thin foils, the applicability of advanced high-angle annular dark-field scanning transmission electron microscopy (HAADF STEM) for atomic displacement and strain analysis was investigated for GPA [38, 42] and PF [42, 43]. Images obtained by HAADF STEM provide for atomic resolution over a large range of specimen thickness, while contrast reversals due to changes in specimen thickness or defocus do not occur and the images can be directly interpreted in terms of atomic column positions. Another advantage is seen in the generally high sensitivity of the image contrast towards the atomic number ( $z$ -sensitivity), thus, providing additional information of the local atomistic composition [42, 44, 45]. However, the lower signal-to-noise ratio, environmental noise as well as flyback errors stemming from beam shifts between individual scanning lines were identified as critical factors for accurate displacement and strain measurements [38, 42, 43].

Different strategies were suggested for eliminating the systematic flyback errors imposed by STEM imaging. Thus, Chung et al. [38] proposed choosing the (fast) scan direction parallel to the direction of the principal strain. Similarly, Zhu et al. [42] took two images of the area of interest (AOI) applying a scan rotation of 90° between the recordings and individually determined the displacements along the two considered lattice directions. However, the applicability of these approaches is questionable, especially when the strain field is not known or strain gradients in multiple image directions are present. For PF, Zuo et al. used a promising numerical correction basing on the determination of the flyback error in an undistorted lattice region and were, thus, able to reduce the error to values less than 1 pixel in both scan directions [43].

While random noise and the comparably low signal-to-noise ratio of STEM images in GPA are effectively dealt with by applying a circular mask around the selected Bragg spots in the Fourier space [10, 11], more complicated filters have to be used for filtering in case of PF techniques, i.e. in real space. Zuo et al. drew on the PF method of template matching (TeMA), which was originally introduced for electron imaging of single biological particles [46], and expanded its applicability towards the determination of displacement and strain fields in crystal structures [43]. By selecting an individual column or a group of columns of atoms as template and cross correlating this template to the AOI, the noise could be filtered out and clearly separated correlation peaks are obtained representing the positions of atomic columns.

### 1.3. Approach of current study

The approach for the current study is derived from prior studies focusing on high resolution displacement mapping. The motivation evoked by the corresponding findings and restrictions is outlined in the following.

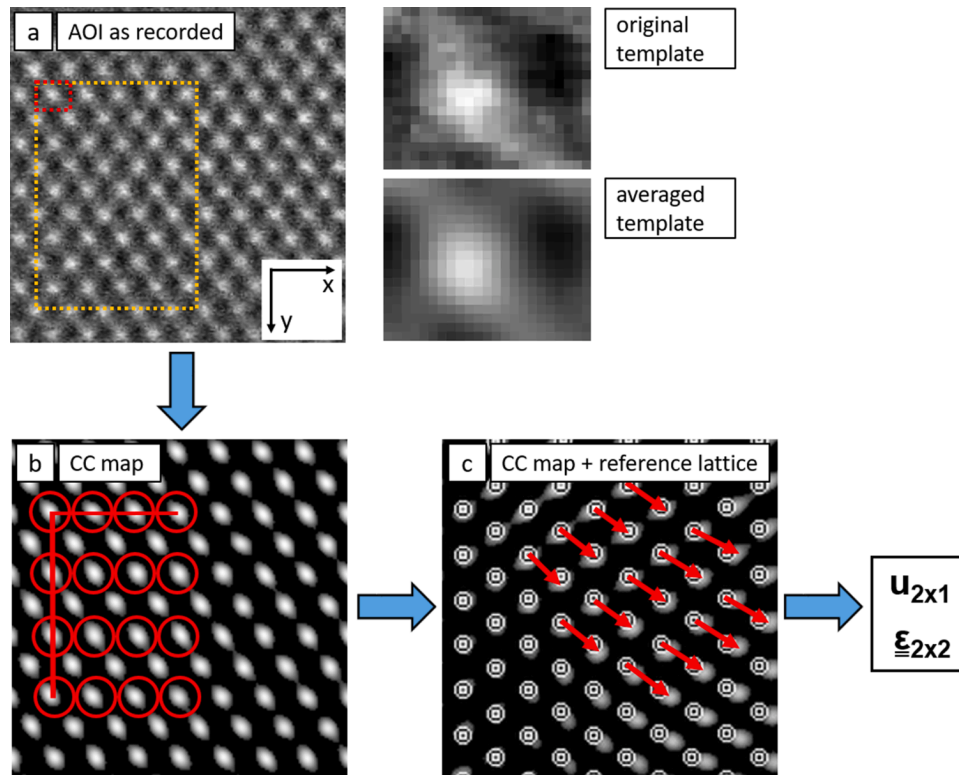


**Fig. 1.** Basis principle and steps of TeMA. (a) Template definition and spatial averaging. (b) Cross correlation and reference lattice definition. (c) Determination of deviations between measured lattice and superimposed reference lattice. The displacements in (c) are indicated by the red arrows, which are exaggerated for visualization purposes.

For both techniques, GPA and TeMA, high accuracies for determination of strains and displacements on basis of STEM images were purportedly reported [38, 42, 43]. However, the purpose of these studies were interfaces within semiconductors and inorganic compounds only, where the local displacements were small. In principle, the capability of GPA for quantification of a full dislocation was shown using a conventional HRTEM image of Si [24]. The Burgers vector was determined through integrals defined on the phase component maps. A similar approach using the Nye-tensor has also been proposed in other studies [21, 28, 47, 48]. While strain-fields around lattice dislocations in metals have been quantified in studies such as [49, 50], the focus has not been to evaluate the Burgers vector from the displacement field. No assertions with respect to the location of the slip plane or the dependence of the magnitude of the induced displacements were made. Also for TeMA, no data on these aspects can be found. Admittedly, these were not the emphasis in the innovative work of TeMA of Zuo et al. [43]. And although the issues caused by large displacements have been previously noted [51], a systematic analysis of their effects in dislocation-characterization has not been done. Thus, the current study addresses this gap by examining the localization and quantification of simulated and actual dislocation-induced high displacements within metallic materials. Using an approach combining simulated images and high resolution STEM images, the applicability and limitations of TeMA are critically examined, while comparisons to GPA are drawn. The susceptibility of both methods to the definition of the unstrained reference lattice is evaluated by choosing a high entropy alloy (HEA) as the material of study, which, due to the presence of a complex multi-element distribution supposedly features strains on the level of individual unit cells. The quantification of defects in this type of material is, therefore, expected to be more delicate in comparison to that of conventional alloys.

## 2. Principle of TeMA

In the following, the principle of TeMA is briefly explained drawing largely on the descriptions by Zuo et al. [43]. For details on individual steps and mathematical formulae the reader is referred to their more comprehensive work focusing on the development of the methodology. A detailed description of GPA is given by, e.g. Hýtch [22], while an illustration of the main steps is provided in Appendix A (Fig. A 1).

The basis for TeMA is an image of the AOI recorded by HRTEM or STEM on a preferably low-indexed zone axis, so that atoms are aligned in columns appearing as individual dots of several pixels in the image plane (Fig. 1(a)). However, in case of as-recorded STEM images, these dots are not clearly separated from the background due to the comparably low signal-to-noise ratio typically present. As this impedes sound peak detection, the template matching procedure is performed, where, in a first step, the template is defined by selection of an individual column or a group of columns within the AOI (red rectangle in Fig. 1(a)). In order to generate a representative template, spatial averaging is conducted. In this step, several sub-images having the same dimensions as the selected template are identified within a specified area (orange rectangle in Fig. 1(a)). The intensity of each pixel of the new, spatially averaged template is then obtained by summing up the corresponding pixel intensities of the sub-images divided by the number of sub-images. The effect of this procedure is illustrated upon comparison of the templates before and after spatial averaging in Fig. 1(a). While the original template features a rather irregular intensity distribution, the averaged template has a clear intensity distribution with maximum values in the center of the column.

Using a cross correlation function, the similarity between the averaged template and a rectangle of identical dimensions is evaluated for each pixel within the AOI. When the congruence between the template and the rastered rectangle is high, which is the case for the positions of individual columns, a high correlation coefficient (CC) is obtained. Vice versa, low or negative values are obtained, when the congruency is low

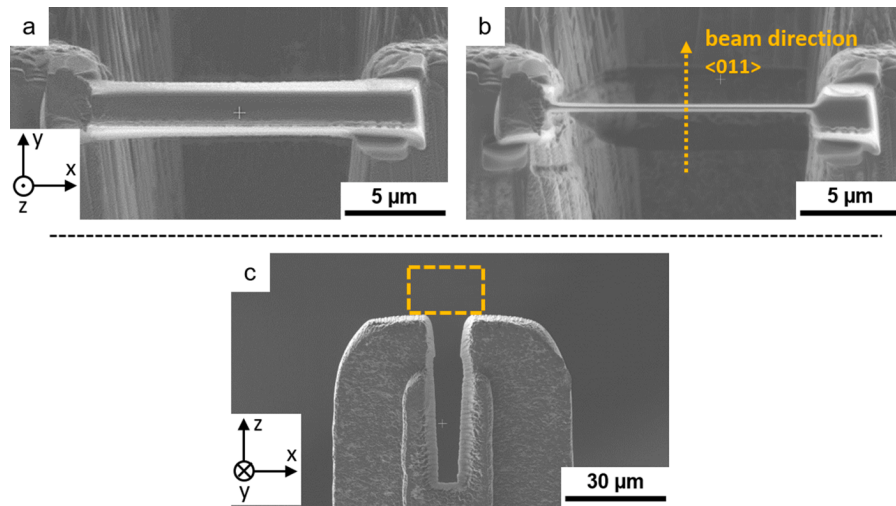


**Fig. 2.** Two-pole specimen preparation by FIB. Top views of (a) the specimen attached to the lift-out grid prior to thinning and (b) of the thinned specimen with remaining solid poles to both sides of the thinned area. (c) Side view of the flattened post of the lift-out grid and milled trench for avoidance of material redeposition during thinning. The later position of the specimen is marked by the orange rectangle. The spatial orientations given in (a) are equally valid for (b).

(in areas featuring noise). After plotting the CC of every pixel and applying a threshold to the obtained map, the positions of atomic columns are represented by local maxima of the CC, clearly separated from the aforementioned noisy background (Fig. 1(b)).

It has to be noted, that the absolute positions of these maxima are shifted with respect to the original atomic columns according to the intensity distribution within the template. However, the relative positions between the individual columns are maintained and, thus, evaluation of the local displacements is not affected. The center of each column is then identified with sub-pixel accuracy using the center of gravity measure, as discussed in detail in e.g. [52].

For definition of the perfectly regular reference lattice, the directions of two base vectors are defined in an unstrained region within the CC map (here along 4 columns in  $x$ - and  $y$ -direction in Fig. 1(b)). This provides a first estimation of the reference lattice with respect to its origin and the two base vectors reflecting the distance to the respective neighboring column in terms of  $x$ - and  $y$ -coordinates. In an iterative refinement procedure the sum of the deviation between the measured column positions and the reference lattice points within the unstrained region is minimized by numerical alteration of the reference lattice parameters. When the best fit is achieved, the final lattice parameters are used for extrapolation of the reference lattice across the entire AOI. TeMA then calculates the displacements  $u_{2 \times 1}$  as local deviation between the measured atomic column positions and the perfectly regular reference lattice (Fig. 1(c)). The strain field  $\underline{\epsilon}_{2 \times 2}$  is obtained by numerical differentiation of the measured displacements. Both displacement and strain fields can be exported as maps, where each pixel refers to an individual atomic column and individual values are reflected by the intensity of each pixel.

### 3. Experimental details

The material investigated is a face centered cubic (FCC) FeCoCrNiMn high entropy alloy (HEA) single crystal of equiatomic composition. Prior to sample extraction for STEM, the material was homogenized (1200 °C/24 h + oven cooling + 1100 °C/1 h + oven cooling) and mechanically compressed to 23% strain with the loading axis parallel to the  $\langle 001 \rangle$  crystal direction. Previous work on the mechanical response of these samples was reported in [53, 54]. A cross section of the specimen was extracted using focused ion beam (Scios 2 Dual-beam FIB-SEM, Thermo Fisher Scientific), such that the  $\langle 011 \rangle$  crystal direction could be aligned parallel to the incident beam during later STEM examination using marginal specimen tilt only.

In order to prevent warpage, the specimen was thinned in the center area only, so that two supporting poles of high thickness remained on both sides of the transparent area (Fig. 2 (a, b)). To achieve this objective, the specimen was attached on top of a single post of the lift-out grid. The post was modified by a prior milling procedure, such that a flat top and an additional trench ensured proper positioning of the specimen and avoidance of material redeposition in course of the subsequent thinning procedure, respectively (Fig. 2(c)).

For recording images at atomic resolution an aberration corrected STEM (Themis Z, Thermo Fisher Scientific) operating at 300 kV was used. The images were recorded with the incident beam parallel to the  $[011]$  zone axis at a resolution of  $2048 \times 2048$  pixels and a dwell time of 8  $\mu$ s. As no scan rotation was applied, the recorded images were digitally rotated and cropped, such that the  $[0\bar{1}1]$  and the  $[100]$  crystal directions were parallel to the horizontal and the vertical image edge, respectively.

In order to enable for critical evaluation of the experimental data as well as for systematic examination of individual phenomena, artificial images featuring known displacement distributions were generated. This was done by applying a known vector displacement field to an undeformed lattice of certain size. The deformed configuration was imported in OVITO [55], an atomistic visualization tool, to generate grayscale images of the deformed lattice projection as viewed along a given zone axis. In correspondence to the lattice spacing of FeCoCrNiMn reported in [56], the virtual crystal was built up with a value of  $d_{001} = 3.528$  Å. The imposed displacement distributions comprised (i) uni-directional displacements in form of an arctangent-function having a maximum displacement of 1 Å and 1.5 Å and (ii) crystal defects in form of a  $[121]$  partial dislocation (Burgers vector length of 1.44 Å) and a  $[\bar{1}01]$  full dislocation (Burgers vector length of 2.50 Å). In accordance to the experimental image, the zone axis of the images corresponds to the  $[011]$  crystal direction, with the image edges aligned parallel to  $[0\bar{1}1]$  and  $[100]$ . In case of the crystal defects additional images were generated with a zone axis of  $[110]$  and the image edges parallel to  $[\bar{1}10]$  and  $[001]$ . The areas envisaged were about  $250$  Å  $\times$   $72$  Å for the arctangent-functions and about  $125$  Å  $\times$   $125$  Å for the dislocations.

The parameters for TeMA analysis were maintained constant in all examinations. The template was extracted across a single column and spatially averaged across an area of  $9 \times 9$  columns in each direction with a threshold of 0.6. The CC map was generated cross correlating the template to the entire AOI with the cross correlation function given in [43] and applying a threshold of 0.2. Subsequently, the reference lattice was defined on the CC map with vectors parallel to  $(011)$  and  $(100)$ . The

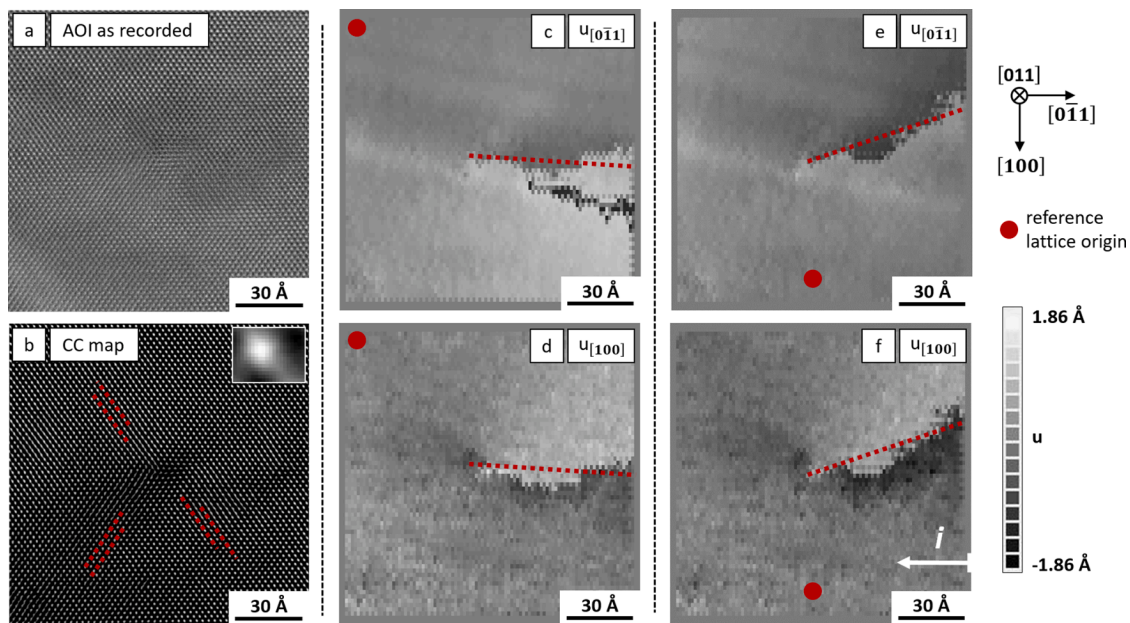


**Fig. 3.** HR-STEM image of the AOI in the as-recorded state (a) and after template matching (b). The inset in (b) is an enlarged image of the spatially averaged template of a single column used for the cross correlation. The displacements in  $[0\bar{1}1]$ - and  $[100]$ -direction obtained by TeMA are given for different referent lattice origins in sub-images (c,e) and (d,f), respectively. In any case, a clear discontinuity in the displacements is present with its average orientation (highlighted by the red dashed lines) depending on the arbitrary chosen reference lattice origin (red dots). The marking  $i$  in sub-image (f) refers to the numbering of pixels along  $[0\bar{1}1]$  used for evaluation of the displacement magnitudes (details see text).

iterative refinement of the lattice parameters was performed in an area of  $11 \times 11$  columns until no changes in the parameters were observed in consecutive steps. The origin of the reference lattice was chosen at different positions within the AOI and is specified in the corresponding images in the results and discussion sections.

Comparative examinations were conducted with GPA using the code provided in [57]. The  $\{111\}$  diffraction spots were chosen for Bragg filtering and subsequent phase analysis. The refinement of the corresponding  $\langle 111 \rangle$  g-vectors was conducted with the reference areas being in correspondence to those of the TeMA analysis. The iterative procedure was carried out until no changes in the g-vector coordinates were observed.

#### 4. Results

The rotated and cropped AOI used for analysis by TeMA and GPA is shown in Fig. 3(a). In the as-recorded state, i.e. when no post-processing subsequent to STEM imaging is conducted, individual columns showing the typical arrangement of a FCC crystal as viewed parallel to a  $\langle 011 \rangle$  zone axis are already visible. Unfortunately, the image is characterized by low signal-to-noise ratio and comparably uneven background contrast, so that distinction of individual columns in certain areas is

insufficient. The effectiveness of template matching with respect to the reduction of noise can be derived from comparison of the initial AOI to the CC map in Fig. 3(b). By cross correlation of the spatially averaged template (inset in Fig. 3(b)) with the AOI, mostly separated columns in front of a uniform, black background are obtained. However, several columns are still interconnected forming slanting lines (highlighted by the dashed red lines), indicating the presence of a defect in the center of the image.

The obtained displacement maps for the two selected lattice vector directions ( $[0\bar{1}1]$  and  $[100]$ ) are given for different reference lattice origins in Fig. 3 (c-f). The maps reveal clockwise decreasing displacements in  $[0\bar{1}1]$ -direction (Fig. 3(c, e)) and clockwise increasing displacements in  $[100]$ -direction (Fig. 3 (d, f)) with the reference lattice origin having starting values of 0 and the center of the rotation coinciding with the center of the image. A discontinuity within these displacement distributions is formed along the line where positive and negative displacements meet. This distribution describes the profile around a dislocation with its displacement discontinuity or disregistry along the slip-plane. However, the orientation of the observed discontinuity line seems not to be related to the actual, physical displacement of the columns, e.g. as induced by a slip plane, but rather to be dependent on the position of the

**Table 1**

Theoretical displacement components in the  $(110)$ -projection  $|u_{[0\bar{1}1]}|$  and  $|u_{[100]}|$  of a full  $a/2(110)$  and partial  $a/6(121)$  dislocation. The relative error of the measured displacement components to the theoretical values is given in the columns  $f_{[uvw]}$ .

possible Burgers vectors		$ u_{[100]} $	$f_{[100]}$	$ u_{[0\bar{1}1]} $	$f_{[0\bar{1}1]}$
$a/2$	$[110], [\bar{1}\bar{1}0], [1\bar{1}0], [\bar{1}10], [101], [\bar{1}0\bar{1}], [10\bar{1}], [\bar{1}01]$	1.764 Å	0.02	1.247 Å	0.05
	$[011], [0\bar{1}\bar{1}]$	0 Å	-	0 Å	-
	$[0\bar{1}\bar{1}], [0\bar{1}1]$	0 Å	-	2.495 Å	0.52
$a/6$	$[121], [1\bar{2}\bar{1}], [112], [1\bar{1}\bar{2}], [\bar{1}21], [\bar{1}\bar{2}\bar{1}], [\bar{1}12], [\bar{1}\bar{1}\bar{2}]$	0.588 Å	2.05	0.416 Å	1.86
	$[12\bar{1}], [1\bar{2}1], [11\bar{2}], [1\bar{1}\bar{2}], [\bar{1}2\bar{1}], [\bar{1}\bar{2}\bar{1}], [\bar{1}1\bar{2}], [\bar{1}\bar{1}\bar{2}]$	0.588 Å	2.05	1.247 Å	0.05
	$[211], [2\bar{1}\bar{1}], [\bar{2}11], [\bar{2}\bar{1}\bar{1}]$	1.176 Å	0.53	0 Å	-
	$[2\bar{1}\bar{1}], [2\bar{1}1], [\bar{2}\bar{1}\bar{1}], [\bar{2}\bar{1}1]$	1.176 Å	0.53	0.832 Å	0.43
	measured displacements	1.795 Å	-	1.189 Å	-

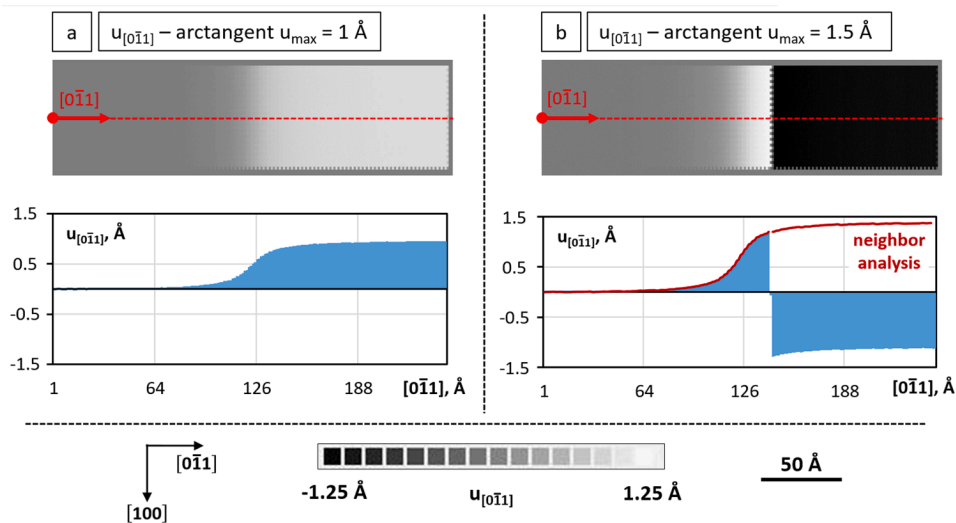


**Fig. 4.** Displacements in  $[0\bar{1}1]$ -direction obtained by TeMA-analysis of the virtual crystal featuring imposed arctangent-displacement-functions with maximum values of 1 Å (a) and 1.5 Å (b). The graphs underneath the displacement maps illustrate the displacement along the red dashed lines in the corresponding maps.

reference lattice origin, as can be derived by comparison of Fig. 3 (c) to (e).

For evaluating the magnitude of the displacements across the discontinuity, the difference between the maximum and minimum values on each side of the discontinuity was examined. In order to account for scatter in the experimental data, the average of  $N = 5$  individual values was calculated according to Eq. (1).

$$\Delta u_{[uvw]} = \sum_{i=5}^{4+N} \frac{u_{[uvw]max,i} - u_{[uvw]min,i}}{N} \quad (1)$$

with  $u_{[uvw]max,i}$  and  $u_{[uvw]min,i}$  being the maximum and minimum values within a single column of pixels  $i$ . The columns are consecutively numbered starting from the right image edge, as indicated by the white arrow in Fig. 3 (f). The values at the very edge of the image were not

included in order to avoid artifacts stemming from TeMA, which can be seen, e.g. in form of the blank values surrounding each map (Fig. 3 (c-f)).

Applying this procedure, values of  $\Delta u_{[0\bar{1}1]} = 1.18$  Å and  $\Delta u_{[100]} = 1.77$  Å were obtained from Fig. 3(e) and (f), respectively. These values were compared to theoretical values of a  $a/2\langle 110 \rangle$  full and a  $a/6\langle 121 \rangle$  partial dislocation on  $\{111\}$  slip planes. Taking into account all possible Burgers vector orientations, the displacement components in the (110)-projection  $|u_{[0\bar{1}1]}|$  and  $|u_{[100]}|$  of each type of dislocation were determined. Table 1 summarizes the magnitudes of possible displacement components together with the relative error  $f_{[uvw]}$  of the measured displacement magnitudes to the theoretical values according to Eq. (2).

$$f_{[uvw]} = \frac{|u_{[uvw]theo} - |u_{[uvw]meas}|}{|u_{[uvw]theo}|} \quad (2)$$

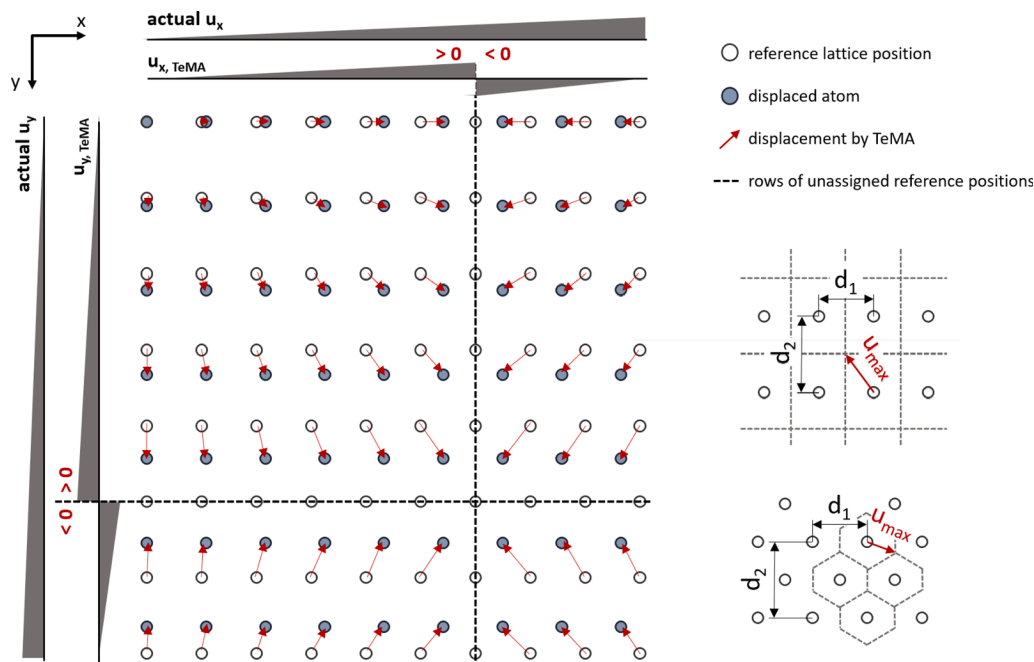


**Fig. 5.** Nearest neighbor assignment of displaced atoms and reference lattice positions for a rectangular lattice projection leading to discontinuities of resulting displacements in x- and y-direction. The schematics to the right illustrate the shape of the Wigner-Seitz cells (rectangle or hexagon) leading to different maximum definite displacements in dependence of the crystal structure and zone axis contemplated (see text for details).

with  $u_{[uvw]}_{theo}$  being the calculated displacement magnitude using the theoretical lattice constant  $a$  of 3.528 Å and  $u_{[uvw]}_{meas}$  being the displacement magnitude determined on basis of TeMA data.

As shown in Table 1, the relative error for the partial dislocations is clearly higher than the error for the full dislocation. Thus, the presence of a full dislocation in the center of the AOI can be derived from the TeMA data and is consequently seen to be the reason for the displacement distribution as observed in Fig. 3 (c-f). The difference of the displacements across the discontinuity line well reflects the displacement induced by the dislocation. However, as outlined above, the orientation of the discontinuity line is not related to the physical displacements but changes with the choice of the reference lattice origin. Consequently, no assertions with respect to the orientation of the Burgers vector or the site of the slip plane can be made and a deeper understanding of TeMA is necessary in order to evaluate its capability for a comprehensive determination of crystal line defects. This will be discussed using simulated displacement distributions in the following section.

## 5. Discussion

### 5.1. Displacement magnitudes

For the analysis of the effect of different displacement magnitudes, the simulated images featuring uni-directional displacements in form of arctangent-functions with different maximum displacements were used. The maps of the corresponding displacements in  $[0\bar{1}1]$  direction as obtained by TeMA are given in Fig. 4.

In the case of the maximum displacement of 1 Å (Fig. 4(a)), the displacement map shows a monotonic distribution with increasing displacements from left to right and the corresponding graph sufficiently reproduces the imposed arctangent-function. However, in the case of higher maximum displacements (Fig. 4(b)), an artifact in the displacement distribution is present in the center of the map, which is reflected in the corresponding graph by an abrupt change from positive to negative displacements. In consequence, the maximum displacement directly ascertainable by TeMA seems to be unsatisfactory. Further artifacts were found to result from improper reference area definition. Thus, if large displacement gradients are included in the area for the reference lattice definition, accordingly averaged displacement values are obtained. Eventually, the displacement mappings are prone to misinterpretation even if the maximum displacement is small. This is exemplarily shown for the arctangent-function with a maximum displacement of 1 Å in Fig. A 2.

This can be explained by the assignment of the displaced atomic columns to individual reference lattice positions, which is in TeMA realized via a nearest neighbor approach. The principle is schematically illustrated in Fig. 5 for a simple rectangle column arrangement, which corresponds to a body centered cubic (BCC) crystal in a  $\{011\}$ -projection and is, in similar fashion, applicable to a BCC and a FCC crystal in a  $\{001\}$ -projection. The more complicated case of a lattice arrangement corresponding to a BCC crystal in a  $\{111\}$ -projection and a FCC crystal in  $\{111\}$ - and  $\{011\}$ -projections is given in the Appendix (Fig. A 3).

To elucidate the effect of the nearest neighbor assignment on the displacements calculated by TeMA, linearly increasing displacements in x- and y-direction are imposed to the crystal (cf. *actual*  $u_x$  and *actual*  $u_y$  in Fig. 5). The assignment of the displaced atoms to the reference lattice positions and according displacements are indicated by the red arrows. As can be clearly seen, a transition from positive to negative displacements is obtained when the imposed displacement exceeds 50% of the lattice spacing in the corresponding direction (cf.  $u_x$ , *TeMA* and  $u_y$ , *TeMA*). In accordance with such a scenario, the discontinuity in case of Fig. 4(b) occurs from a displacement of 1.295 Å to  $-1.20$  Å, reflecting a jump from 50% to  $-50\%$  of the lattice spacing in  $[0\bar{1}1]$  direction (2.495 Å).

The area around an individual reference lattice position, in which a displaced column can be unambiguously assigned to that position, is

describable by the Wigner-Seitz cell of the real-space reference lattice at that position. Following the dependence of the projection itself, the size and shape of this cell depend on the crystal parameters (crystal structure and lattice constants) and the zone axis envisioned. The different Wigner-Seitz cells resulting from two prominent column arrangements (rectangular and hexagonal) are given in the schematics to the bottom right of Fig. 5, where the maximum definite displacement  $u_{max}$  can be determined in dependence of the lattice distances  $d_1$  and  $d_2$  in the projection.

This limitation is similarly observed in GPA, although this method works in reciprocal space and the underlying mechanism is different. In GPA, the displacements at the position are calculated on basis of phase distribution  $P_g(\mathbf{r})$  of the reciprocal lattice vector  $g$ . This phase distribution reflects the local deviation of the position of the lattice planes in real space, i.e. the lattice planes corresponding to  $g$ , relative to the position of the (undeformed) reference lattice planes. The deviation is normalized between  $+\pi$  and  $-\pi$  [22, 23]. For a visual interpretation of the principle, the reader is referred to Fig. A 1. The relation between the displacement component  $u_1(\mathbf{r})$  in the direction of the reciprocal lattice vector  $g_1$  and the phase  $P_{g_1}(\mathbf{r})$  is given by:

$$u_1(\mathbf{r}) = -\frac{P_{g_1}(\mathbf{r})}{2\pi g_1} \quad (3)$$

With  $g_1 = \frac{1}{d_1}$ , the maximum displacement in direction of  $g_1$  is limited to  $\frac{d_1}{2}$ . A linearly increasing displacement in direction of the reciprocal lattice vector is consequently unambiguously determined as long as the distance to the next reference plane is smaller than  $\frac{d_1}{2}$ . Upon exceeding this limit, the displacement jumps by  $-d_1$  (to a negated value), following which the increasing trend is continued. The effect is demonstrated by Hýtch et al. [23] using the example of a PbTiO<sub>3</sub> domain wall, where a difference between the reciprocal lattice vectors of the two domains is existent. This can be interpreted via a linearly increasing displacement upon crossing the interface. Consequently, the phase images revealed repeating ramps ranging from  $-\pi$  to  $\pi$  on one side of the interface.

The similarity of TeMA and GPA with respect to this effect, i.e. the presence of a crystal and projection dependent limitation of maximum definite displacements, was confirmed by GPA analysis of the virtually generated crystal featuring the imposed arctangent-displacement-functions, which revealed displacement maps and graphs identical to those obtained by TeMA (not shown for sake of brevity).

However, although the displacements beyond the threshold are not directly obtained in a correct fashion, the information of the actual displacements is still reflected by the magnitude of the negative displacements. Thus, the actual displacement can be corrected by post-processing of the original data in form of e.g. a nearest neighbor analysis. For the very simple case of uni-directional displacements limited to 1.5 Å, this was realized via Eq. (4).

$$u_{[uvw],i} = \begin{cases} u_{uvw,i} & \text{for } u_{uvw,i} - u_{uvw,i-1} \leq d_{uvw}/N \\ u_{uvw,i} + d_{uvw} & \text{for } u_{uvw,i} - u_{uvw,i-1} \geq d_{uvw}/N \end{cases} \quad (4)$$

For  $[uvw] = [0\bar{1}1]$ ,  $d_{[0\bar{1}1]} = 2.495$  Å and  $N = 10$ , the red graph in Fig. 4 (b) was obtained, which clearly traces the imposed arctangent-function.

The aspects outlined above illustrate the effect of the nearest neighbor assignment in case of simple, uni-directional displacement functions on a rather qualitative basis. For a more comprehensive description on mathematical grounds and for arbitrary 2D-displacements, the reader is referred to Appendix B.

### 5.2. Dislocation analysis

Due to the limitation in ascertainable displacements, the quantification of crystal defects using TeMA might be impeded. In order to get a deeper understanding of the impact of this limitation in these cases, the virtual crystals featuring a full  $\frac{a}{2}[\bar{1}01]$  and a partial  $\frac{a}{6}[121]$  dislocation

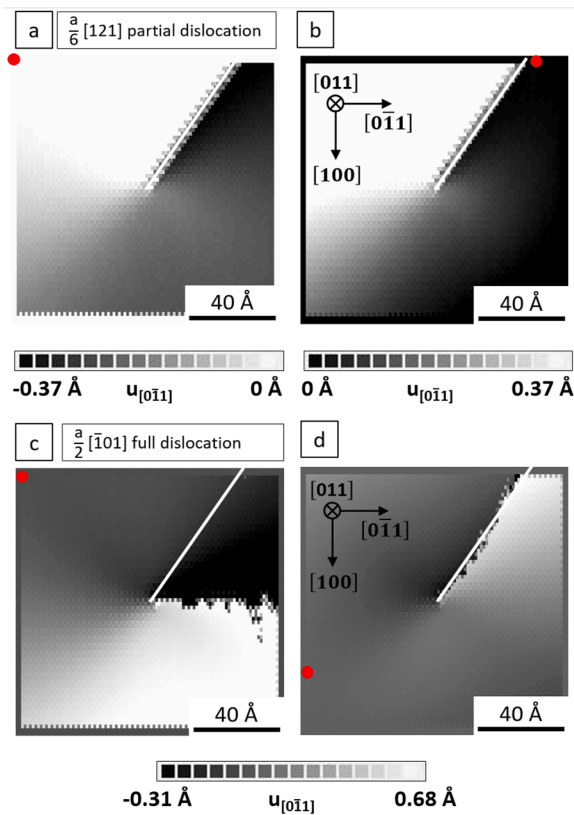


**Fig. 6.**  $[0\bar{1}1]$ -Displacement maps obtained by TeMA on virtual crystal featuring a  $\frac{a}{6}[121]$  partial dislocation (a,b) and  $\frac{a}{2}[\bar{1}01]$  full dislocation (c,d) for different reference lattice origins indicated by the red dots. The site of the dislocation plane as known from the simulation is indicated by white solid lines.

were analyzed. Both dislocations lie on the  $(1\bar{1}1)$  slip plane. The displacement fields were determined from linear anisotropic elasticity, following the Eshelby-Stroh formalism [58]. With Burgers vectors of 2.495 Å and 1.176 Å for  $\frac{a}{2}[\bar{1}01]$  and  $\frac{a}{6}[\bar{1}01]$  respectively, the magnitude of the induced displacements is clearly different and exceeding the lattice spacing in some directions. Thus, an effect on the final displacement fields obtained from TeMA or GPA is expected. The displacements in  $[0\bar{1}1]$  direction obtained by TeMA are shown in Fig. 6 for the different types of dislocations and different reference lattice origins.

An important observation is, that while the  $\frac{a}{6}[121]$  partial dislocation (Fig. 6 (a,b)) induces a clockwise increasing displacement around the center of the defect, i.e. at the site of the dislocation core, the opposite trend is observed for the  $\frac{a}{2}[\bar{1}01]$  full dislocation (Fig. 6(c)). By choosing the reference lattice origin at a specific site, the displacements at that site are set to zero and the precise values in the remaining areas are plotted relative to this origin. Thus, the qualitative displacement distributions as an outcome of TeMA are not affected, as can be clearly seen by comparing Fig. 6(a) and (b), where the scales were adjusted according to the different reference lattice origins and the qualitative displacement distributions are identical.

From theory, the dislocation slip plane hosts a discontinuity in the displacement field across it. The location is known from the imposed displacement fields and highlighted by the white lines in Fig. 6. However, the slip plane is detected in case of the partial dislocation only. Irrespective of the reference lattice origin, it is indicated by a sharp transition line from positive to negative displacements (Fig. 6 (a,b)). This is not observed in case of the full dislocation. Although a discontinuity in the displacements is present, the site of the corresponding line depends on the site of the reference lattice origin, which is why an agreement to the dislocation plane is not obtained in most cases (e.g. Fig. 6(c)). Still, the origin might, by coincidence, be chosen aptly such that an agreement is observed (Fig. 6(d)). However, this is not to be mistaken for a physical relation between these types of lines. A mathematical explanation for the generation of the discontinuity and the dependency of its site on the reference lattice origin is provided in

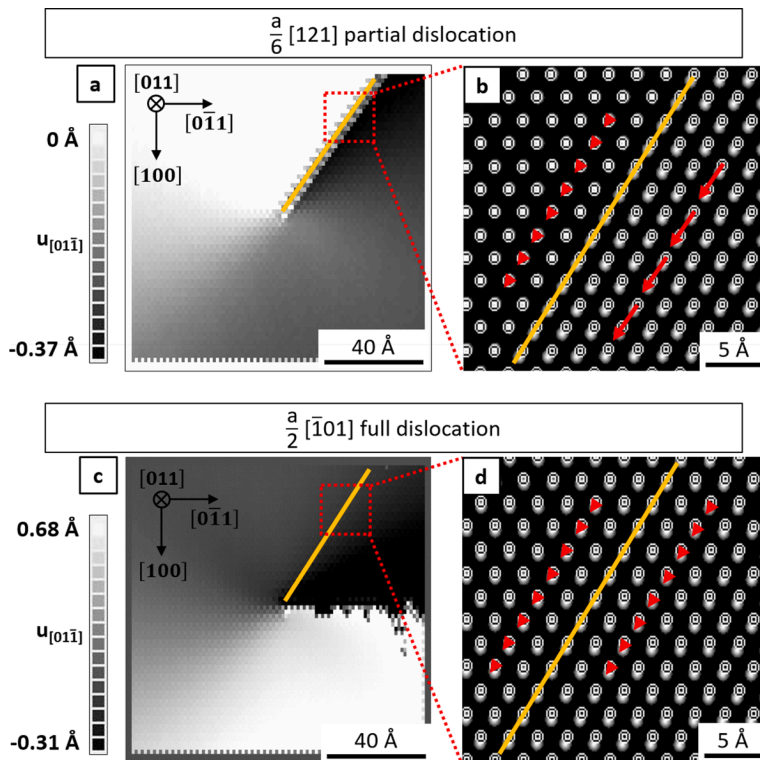


**Fig. 7.** Detection of the additional half plane (solid orange lines) in dependence of the displacement magnitude induced by the crystal defect. In case of the  $\frac{a}{6}[121]$  partial dislocation, an abrupt change in displacements across the half plane is observed (indicated by enlarged red arrows in the cross correlation map (b)). The site of the half plane is accordingly visualized by an abrupt change in displacements in the displacement map (a). As the lattice is shifted by an entire lattice spacing (100%) by the  $\frac{a}{2}[\bar{1}01]$ -dislocation, the half plane is not captured by TeMA (d) and the site of the half plane and the discontinuity of the displacements do not match (c).

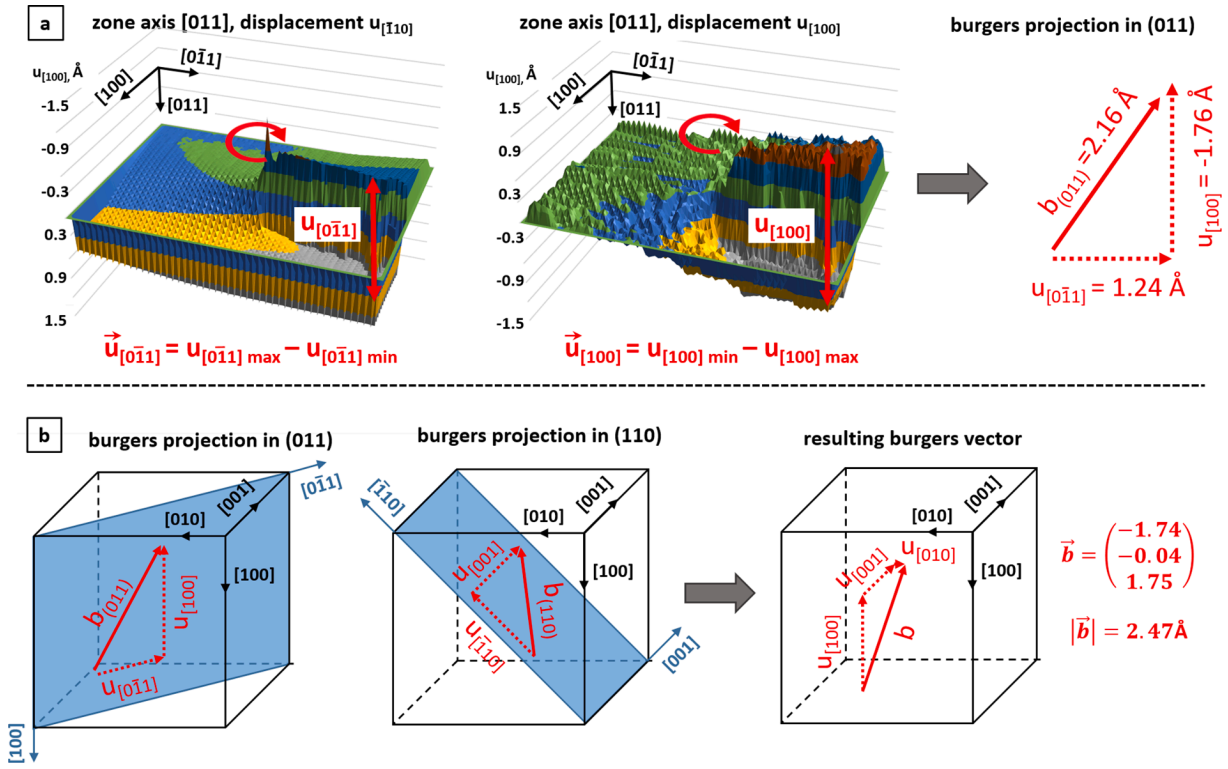


Fig. 8. Methodology for determination of the Burgers vector. (a) Calculation of the Burgers vector projection for a designated zone axis from maximum and minimum displacements across the discontinuity. (b) Construction of the actual Burgers vector from two different projections. The resulting values of  $\vec{b}$  on the right in subimage (b) are derived from the projections in the (011) and (110) plane.

### Appendix C.

Following the discussions of section 5.1, it may seem that the differences in detectability of the dislocation planes are due to the difference in the Burgers vectors together with the inherent limitation of maximum ascertainable displacements. Thus, the displacement induced by the partial dislocation of  $1.176 \text{ \AA}$  is within the Wigner-Seitz-cell of the underlying FCC crystal in the [011] zone axis, while the displacements of  $2.495 \text{ \AA}$  induced by the full dislocation is out of bound. However, as was observed in case of the arctangent-displacements in Fig. 4, a discontinuity should be present at the site where the displacements exceed the limit. As this is not observed in case of the full dislocation (no agreement of the dislocation plane and the discontinuity in Fig. 6(c)), a different effect comes into play. Contemplating the positions of individual atomic columns across the dislocation plane, an abrupt deviation of individual columns and the reference lattice positions in the magnitude of several pixels can be observed in case of the partial dislocation (Fig. 7(b)). This deviation is highlighted accordingly by a sudden change in displacements (Fig. 7(a)). However, as the shift of columns in case of the full dislocation amounts to a full lattice spacing (interpretable as an entire additional lattice plane), the displaced columns are coincident with the reference lattice positions and no sudden change across the dislocation plane is observed ((Fig. 7(d)). Eventually, the dislocation plane cannot be ascertained using TeMA. Hence, the nature of the dislocation itself (being a full lattice dislocation and not a partial one) is also a contributing factor for unambiguous defect characterization.

The effects described above are in similar way applicable to GPA as well. Instead of a deviation of displaced atoms to reference lattice positions, a shift between local lattice plane fringes and reference plane fringes is used for calculation of the displacement fields. In case of the  $\frac{a}{6}[121]$  partial dislocation a clear shift is observed at the dislocation plane, while the  $\frac{a}{2}[\bar{1}01]$ -dislocation again undergoes a shift by 100% and is, thus, not detected. Consequently, the displacement maps obtained by GPA resemble those obtained by TeMA (cf. Fig. 6 and A 4).

However an additional phenomenon in form of sharp discontinuities in some areas of the AOI is visible in Fig. A 4. While this is expected and in accordance to the results of TeMA for the full dislocation (Fig. A 4 (c, d)), the case of the partial dislocation is different (Fig. A 4 (a,b)). Measuring the difference across the discontinuity in Fig. A 4(a) values of  $1.24 \text{ \AA}$  are obtained. This corresponds to the  $[0\bar{1}1]$ -component of one  $\langle 111 \rangle$  g-vector for a phase shift between  $+\pi$  and  $-\pi$ , with the component of the second  $\langle 111 \rangle$ -g-vector being close to zero. Several of these transitions can be observed, when the displacement gradients are small and a phase fluctuates around  $+\pi$ . However, this can be avoided by slightly changing the area for g-vector refinement, i.e. the reference area, such that the phase shift is observed in one direction only. Still, this shows the high sensitivity of GPA towards the definition of the area of reference, as also discussed by [42], resulting in generation of artifacts in the displacement distributions, eventually impeding recognition of the features of interest (Fig. A 5).

Comparing the displacement fields obtained from the virtual crystal (Fig. 6 (c,d)) to the experimentally obtained counterparts (Fig. 3 (c,e)) a high accordance in terms of both the clockwise decreasing  $[0\bar{1}1]$  displacements and the dependency of the discontinuity line from the reference lattice origin becomes clear. As the spatial orientations in the simulated images are identical to those of the experimental image, the nature of the experimentally observed defect resembling a full dislocation is confirmed by this on a qualitative basis.

Still, the orientation of the dislocation plane and thus the direction of the Burgers vector cannot be determined in a straightforward fashion at this point. Thus, a methodology for determination of the Burgers vector comprising both, the magnitude and its orientation was developed. The procedure relies on the contemplation of the obtained displacement components in direction of the reference lattice vectors, their relation to the Burgers vector projections and the determination of the actual Burgers vector from two projections. The principle is illustrated in Fig. 8 for the more critical case of a full dislocation and on basis of TeMA data.

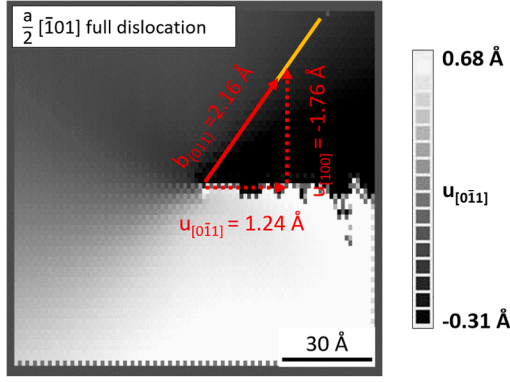


Fig. 9. Burgers vector projection obtained by vectorial evaluation of displacement vectors and site of the simulated dislocation plane (orange line) of the  $\frac{a}{2}[\bar{1}01]$  full dislocation.

However, the procedure is equally applicable to partial dislocations and displacement data obtained by GPA, as will be shown in the remainder of this paper.

For determination of the Burgers vector, the fact that the discontinuity does not reflect the site of the dislocation plane is not considered. However, although a displacement gradient across the entire AOI is observed (clockwise or counterclockwise increasing displacements), the difference between the displacements across the discontinuity is assumed to reflect the maximum displacement induced by the dislocation (for the mathematical proof of the validity of this assumption the reader is referred to Appendix C). A vectorial expression of this difference is obtained by drawing a circle around the dislocation core in analogy to the Burgers vector circuit (red circular arrows in Fig. 8(a)). The displacement vector  $\vec{u}_{[uvw]}$  then is calculated by

$$\vec{u}_{[uvw]} = u_{[uvw]start} - u_{[uvw]end} \quad (5)$$

In order to account for scatter, the start and end values are calculated as average across  $N = 5$  pixels according to Eq. (6).

$$u_{[uvw]start} = \begin{cases} \frac{\sum_{i=5}^{4+N} u_{[uvw]max,i}}{N} \\ \frac{\sum_{i=5}^{4+n} u_{[uvw]min,i}}{N} \end{cases}$$

$$u_{[uvw]end} = \begin{cases} \frac{\sum_{i=5}^{4+N} u_{[uvw]min,i}}{N} \text{ for } u_{[uvw]bottom} \geq u_{[uvw]top} \\ \frac{\sum_{i=5}^{4+N} u_{[uvw]max,i}}{N} \text{ for } u_{[uvw]bottom} \leq u_{[uvw]top} \end{cases}$$

with  $u_{[uvw]bottom}$  and  $u_{[uvw]top}$  being arbitrary displacements on the bottom and the top side of the discontinuity, respectively.

In order to avoid gradient displacements, which are present within short range of the dislocation core, the coordinate  $i$  has to be chosen, such that the displacements across the discontinuity in largest possible distance to the dislocation core are evaluated. This is achieved by selecting the origin of  $i$  at the image edge which features the discontinuity and the direction of  $i$  perpendicular to that edge (cf. white marking in Fig. 3 (f)). In dependence of the direction of  $i$ , the values of  $u_{[uvw]max,i}$  and  $u_{[uvw]min,i}$  are then the maximum and minimum values, respectively, along a single column (for  $i$  parallel to the horizontal image edge) or along a single row of pixels (for  $i$  parallel to the vertical image edge).

Additionally, the comparably high scatter between neighboring values within the displacements in y-direction ( $[100]$ ) has to be noted. In order to provide remedy for this, the displacements in y-direction of each atomic column were averaged across the four nearest neighbors (in  $[100], [\bar{1}00], [0\bar{1}1]$  and  $[0\bar{1}\bar{1}]$  directions). The reasons and an alternative solution for this issue will be discussed after demonstration of the methodology.

Applying the procedure above to the digitally generated images for the  $\frac{a}{2}[\bar{1}01]$  full dislocation as viewed in the  $[011]$  zone axis, a vector  $\vec{u}_{[0\bar{1}1]}$  reflecting a displacement of  $u_{[0\bar{1}1]} = 1.24 \text{ \AA}$  and a vector  $\vec{u}_{[100]}$  reflecting a displacement of  $u_{[100]} = -1.76 \text{ \AA}$  are obtained (Fig. 8 (a)). The addition of both vectors provides the projection of the Burgers vector in the  $(011)$  plane as illustrated in Fig. 8 (a, b). It has to be noted, that the angle of that Burgers vector projection with respect to the image horizontal is  $54.8^\circ$ , which accurately reflects the projection of the simulated dislocation plane ( $1\bar{1}1$ ) at  $54.7^\circ$  (cf. Burgers vector projection and orange lines in Fig. 9). Furthermore, the site of this plane relative to the dislocation core is given by the positive direction of the Burgers vector projection. Thus, the dislocation plane in the observed projection can be directly obtained from the proposed approach (Fig. 9).

For determining the orientation of the actual Burgers vector in space, an additional projection has to be determined. This was conducted for a simulated image of the same  $\frac{a}{2}[\bar{1}01]$  full dislocation viewed in the  $[110]$  zone axis, resulting in the Burgers vector projection in the  $(110)$  plane as also illustrated in Fig. 8(b). On basis of both projections the actual Burgers vector is calculated by solving Eq. (7).

$$\begin{bmatrix} 0 & -1/\sqrt{2} & 1/\sqrt{2} \\ 1 & 0 & 0 \\ -1/\sqrt{2} & 1/\sqrt{2} & 0 \\ 0 & 0 & 1 \end{bmatrix} \begin{bmatrix} b_{100} \\ b_{010} \\ b_{001} \end{bmatrix} = \begin{bmatrix} u_{[0\bar{1}1]} \\ u_{[100]} \\ u_{[\bar{1}10]} \\ u_{[001]} \end{bmatrix} \quad (7)$$

with  $b_{100}, b_{010}, b_{001}$  being the Burgers vector components in the three crystal directions  $[100], [010]$  and  $[001]$ . It has to be noted that Eq. (7) is an overdetermined system, such that definite Burgers vector determination is not possible (presuming scatter is always present in

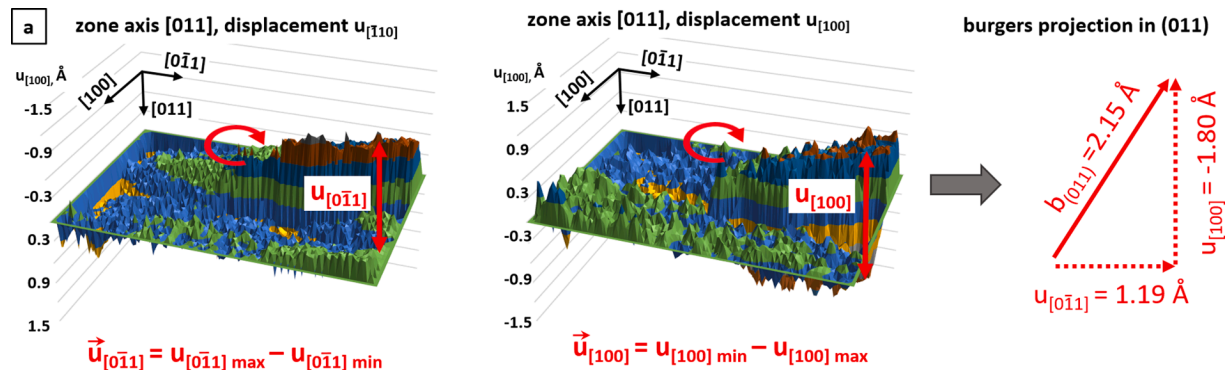
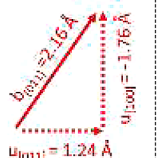
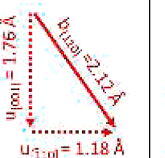
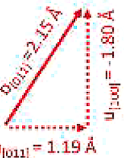
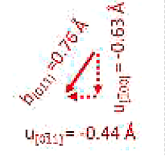
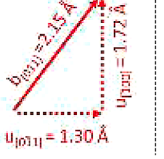
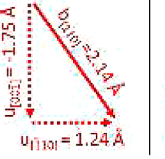


Fig. 10. Burgers vector projection in the  $(011)$  plane as obtained by TeMA analysis of the experimental STEM-image shown in Fig. 3(a).

Table 2

Displacement vectors and resulting Burgers vector projection for two virtually generated projections of the  $\frac{a}{6}[121]$  partial dislocation and the  $\frac{a}{2}[\bar{1}01]$  full dislocation as obtained by TeMA and GPA. The projections derived from corresponding analyses of the experimental image are given to the very right.

	$\frac{a}{6}[121]$ partial dislocation		$\frac{a}{2}[\bar{1}01]$ full dislocation		Experiment
	(011) projection	(110) projection	(011) projection	(110) projection	
TeMA					
GPA					

experimental data). Thus, the Burgers vector can be determined as the best approximate solution to Eq. (7) only. By doing so, a Burgers vector of  $\vec{b} = \begin{pmatrix} -1.74 \\ -0.04 \\ 1.75 \end{pmatrix} \text{Å}$  with a length of  $|\vec{b}| = 2.47 \text{Å}$  is obtained for the  $[\bar{1}01]$  full dislocation, which is in good accordance to the theoretical values of  $\vec{b}_{theory} = \begin{pmatrix} -1.76 \\ 0 \\ 1.76 \end{pmatrix} \text{Å}$  and  $|\vec{b}_{theory}| = 2.49 \text{Å}$ . The deviation in orientation is  $1.0^\circ$  and the normalized deviation in length is 1.0%.

Applying this methodology for the experimental image, displacement vectors of  $\vec{u}_{[011]}$  with a length of  $1.18 \text{Å}$  and  $\vec{u}_{[100]}$  with a length of  $1.79 \text{Å}$  are obtained (Fig. 10). This is in very close agreement to the Burgers vector projection derived from the simulated image and, thus, shows the applicability of the methodology to actual HR STEM images featuring a low signal-to-noise ratio. Additionally, the nature of the experimentally observed defect to be a  $\frac{a}{2}[\bar{1}01]$  full dislocation is clearly confirmed at this point on a quantitative basis. The circumstance that the material considered is a HEA apparently does not significantly deteriorate the accuracy of TeMA, as can be seen by the high accordance of the values of the Burgers vector projection given in Fig. 8 and 10. This might be surprising as this class of material is expected to show local lattice-distortions due to the special alloying concept [59]. Consequently, accurate reference lattice definition might assumed to be problematic because an actually unstrained region cannot be clearly identified. However, at current state an experimental proof of local lattice strains in HEAs is lacking and the general validity of this hypothesis is still questionable [60, 61]. Furthermore, the reference lattice defined in case of the current study might, by chance, be a correct representation of an unstrained region leading to accurate displacements. However, detailed analysis of these phenomena were out of the scope of the current study and, thus, need to be addressed in future work, e.g. by accompanying analysis of the atomic number of individual lattice points.

The methodology described above was furthermore applied to the displacement maps obtained by TeMA of two simulated projections of the  $\frac{a}{6}[121]$  partial dislocation and to the displacement maps obtained by GPA of all types of simulated images and of the experimental image. In case of the latter, a very high agreement between the results from TeMA and GPA is observed, as can be seen by comparison of the displacement maps and derived Burgers vector projections in Fig. 10 and A 6. The values of the Burgers vector projections resulting from TeMA and GPA analyses from all types of images are summarized in Table 2.

Irrespective of the technique applied, a high accordance is observed

in case of the  $\frac{a}{2}[\bar{1}01]$  full dislocation and the experimental image. However, in case of the  $\frac{a}{6}[121]$  partial dislocation, the results from TeMA and GPA clearly deviate. To find an explanation for this, the corresponding 3-dimensional Burgers vectors were calculated according to Eq. (7) using the individual displacements of  $\vec{u}_{(110)}$  and  $\vec{u}_{(100)}$  of the two projections in Table 2. The comparison of the resulting Burgers vectors to the theoretical counterpart shows a deviation in length of 26.9% in case of TeMA and of 6.2% in case of GPA, revealing a higher plausibility of the latter. As the displacement components in (110) directions are virtually identical for both techniques, the reason for the high error of the vector determined by TeMA is seen to be rooted in the displacements in the  $\langle 100 \rangle$  directions. As outlined above, this is the direction, where high scatter between neighboring atomic columns was observed and an averaging procedure was applied. However, this averaging seems to be effective in case of overall large displacements, as present for the  $\frac{a}{2}[\bar{1}01]$  full dislocation, only.

As the scatter is not present when GPA is applied, this phenomenon seems to be rooted in specifics related to the TeMA code. However, no such effects were reported in the original work of Zuo et al. [43]. These authors studied a rectangular atomic column arrangement only, which is a more simple case in comparison to the hexagonal arrangement in case of the current study. Thus, an alternative solution to the issue of scatter is suggested in form of a masking procedure of the atomic columns in the center positions, which stem from the face sides of the FCC crystal. By removing these columns in the raw images prior to TeMA analysis, a significant reduction in the scatter between neighboring atomic columns is achieved. Consequently, the Burgers vector projections of the  $\frac{a}{6}[121]$  partial dislocation were determined to much higher accuracy, while the projections of the  $\frac{a}{2}[\bar{1}01]$  full dislocation are changed to minor extent only (Table A2). Although, the procedure of removal of atomic columns seems applicable to both simulated and experimental images, the exact reason for the scatter observed in case of the hexagonal column arrangement is not clear at this point and, thus, needs to be addressed in future work.

With respect to practical limitations of the suggested methodology, the analysis of two different projections might be challenging. As the TEM samples are obtained by destructive specimen preparation (FIB), two projections of an individual dislocation can be obtained only by tilting the specimen stage within the microscope. However, obtaining proper images at atomic resolution is then impeded, as the effective specimen thickness increases with increasing tilting angles. Additionally, the zone axis cannot be chosen arbitrarily, as the dislocation plane needs to be on-edge in order to obtain clearly separated atomic columns

for evaluation of the displacements across the discontinuity. Furthermore, the achievable tilting angles are kinematically limited by the specimen stage of the microscope used. As remedy, extracting two TEM lamellae with different orientation from the specimen might be considered. However, the equivalence of the characteristics of two individual dislocations is questionable and cannot be assured in a straightforward fashion. However, despite these experimental restrictions, the results prove TeMA as powerful tool for determination of atomistic displacements on basis of HR STEM images featuring a low signal-to-noise ratio. Although a principle limitation with respect to directly ascertainable maximum displacements is present, local displacements amounting up to a full lattice spacing can be analyzed on basis of a vectorial construction of individual displacement components. Using the introduced methodology, both the magnitude as well as the direction of the Burgers vector of different kinds of dislocations can be reliably determined. The site of the dislocation plane is directly obtained in case of small displacements (partial dislocations) or can be derived from the Burgers vector direction with respect to the dislocation core in case of displacements amounting to 100% of the lattice spacing (full dislocations). The procedure is in identical fashion applicable to data obtained by GPA, revealing a high accordance of the Burgers vectors determined by both techniques.

## 6. Conclusions

In the current study, different atomic-scale displacement analysis techniques were examined with respect to their applicability for dislocation characterization in HR STEM images of HEAs. The study draws from the recently introduced real space technique of template matching (TeMA) and provides comparisons to the more established reciprocal space technique of geometric phase analysis (GPA). By recognizing crystal dislocations evoking clearly different displacement magnitudes on basis of both simulated as well as experimentally obtained images comprehensive insights into the specifics of these techniques are obtained. The main conclusions can be summarized as follows:

- Both techniques have an inherent limitation with respect to the maximum unique ascertainable displacement, which depends on the type of crystal structure and zone axis contemplated. In case of TeMA this is due to a nearest neighbor assignment between displaced atoms and reference lattice positions. In analogy to that, GPA features a

limitation of the phase shift between  $++\pi$ . Unphysical jumps in displacements are indicative of related errors and can be circumvented by post-processing of the data in form of a nearest neighbor correction.

- In case of displacements deviating from 100% of the lattice spacing, as induced by e.g. a partial dislocation, the site of the dislocation plane is directly obtained from the displacement maps. When the displacements amount to 100% of the lattice spacing, as evoked by a full dislocation, the dislocation plane is not obtained directly and a discontinuity line is generated in the displacement maps opposite to the site of the reference origin (having displacements of zero).
- The Burgers vector projection on the plane of interest can be determined for any kind of dislocation by vectorial analysis of the displacements, either across the dislocation plane or the discontinuity line. The projection directly indicates the site of the dislocation plane even in case of full dislocations. Using two different projections provides the Burgers vector in 3-dimensional space revealing a high accordance between the results obtained by TeMA, GPA and analytical solutions.
- Applying the suggested methodology to an experimentally obtained atomic-resolution image of HEA proved the general applicability to HR STEM images featuring a relatively low signal-to-noise ratio. The determination of the Burgers vector projection was not found to be critically curtailed by possible lattice distortions within the HEA.

## Declaration of Competing Interest

None.

## Acknowledgements

We note that the authors F. Brenne and A.S.K. Mohammed contributed equally to this paper. The authors thank Prof. Jian-Min Zuo and Mr. Haw-Wen Hsiao for providing the TeMA code and experimental assistance. This work is supported by the Air Force Office of Scientific Research (AFOSR) under award number FA9550-18-1-0198, with Dr. Ali Sayir as Program Director, which is gratefully acknowledged. Sample preparation by FIB and analysis via STEM were carried out in the Frederick Seitz Materials Research Laboratory Central Research Facilities, University of Illinois.

## Appendix A. Figures and tables

The following figures are provided to support our explanations and statements made throughout the manuscript. According references are made in the main text.

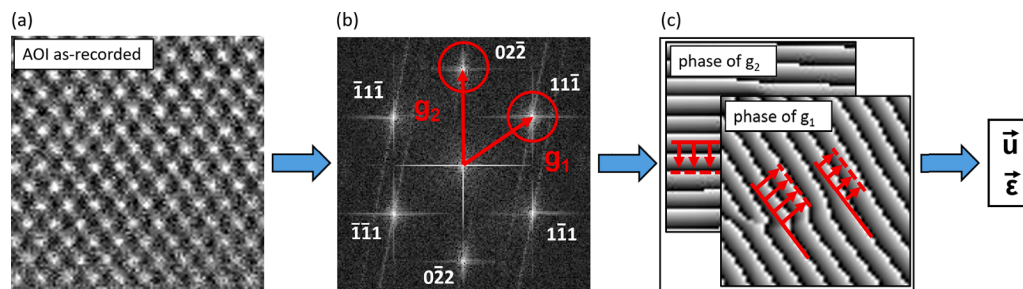


**Fig. A1.** Principle of GPA. (a) Fast Fourier transformation of the as-recorded image of the AOI. (b) Definition of non-collinear vectors  $g_1$  and  $g_2$  and filtering using a Gaussian mask (red circles). (c) Analysis of the local shift, i.e. the phase of the complex Fourier coefficient, of the lattice planes corresponding to  $g_1$  and  $g_2$  (indicated by the red arrows, exaggerated for visualization purposes). The shifts are converted to the displacement field  $u_{2 \times 1}$ , whose derivation provides the strain field  $\underline{\epsilon}_{2 \times 2}$ .

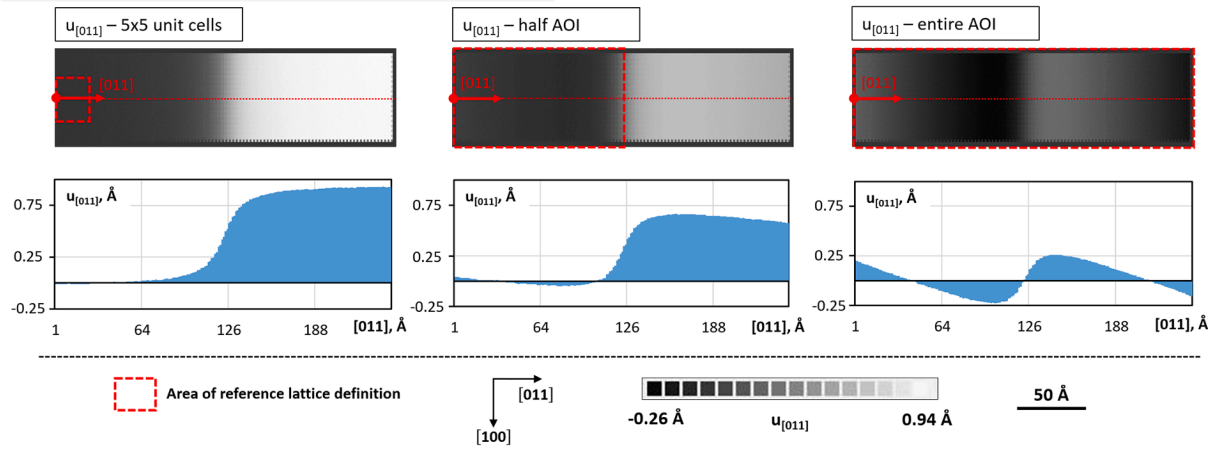


**Fig. A2.** Influence of different area sizes for definition of the reference lattice in TeMA on the resulting displacement distributions. The displacements in  $[0\bar{1}1]$ -direction were obtained by TeMA analysis of the virtual crystal featuring an imposed arctangent-displacement-function with a maximum displacement of  $1 \text{ \AA}$  using the reference areas as indicated in the maps by the red dashed rectangulars. The graphs underneath the maps illustrate the displacement along the corresponding red dotted lines.

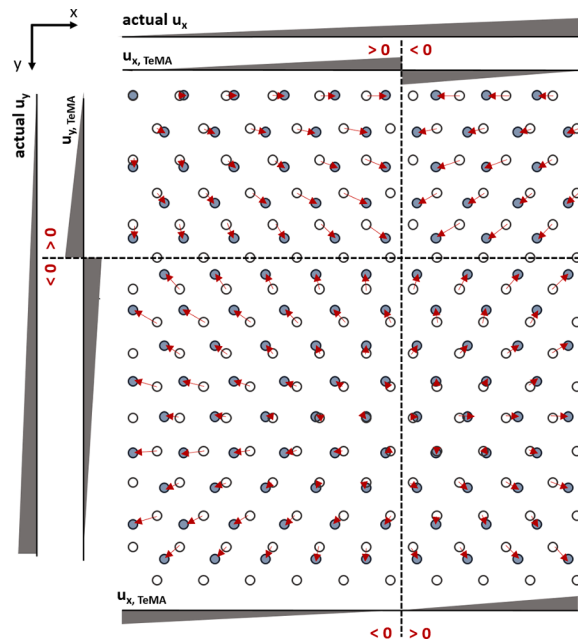


**Fig. A3.** Nearest neighbor assignment of displaced atoms and reference lattice positions in TeMA leading to discontinuities of resulting displacements in x- and y-direction. Note that, in contrast to the rectangular lattice projection (Fig. 5), the transition from positive to negative displacements in y-directions leads to an additional conversion of the displacements in x-direction in case of the more complicated arrangement shown here.

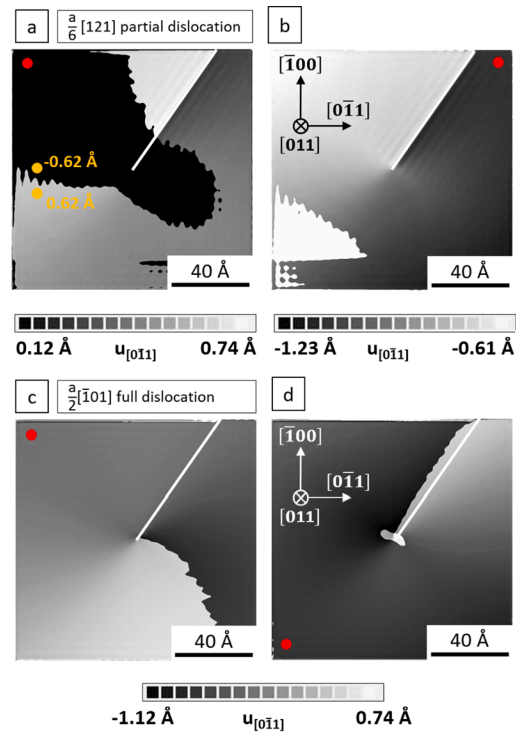


Fig. A4.  $[0\bar{1}1]$ -displacement maps obtained by GPA on virtual crystal featuring a  $\frac{a}{6}[121]$  partial dislocation (a,b) and a  $\frac{a}{2}[\bar{1}01]$  full dislocation (c,d) for difference reference lattice origins indicated by the red dots. The site of the additional half plane as known from the simulation is indicated as white solid line. The orange markings in (a) indicate the local difference in displacements due to  $a \pm \pi$ -phase transition (see main text for details).

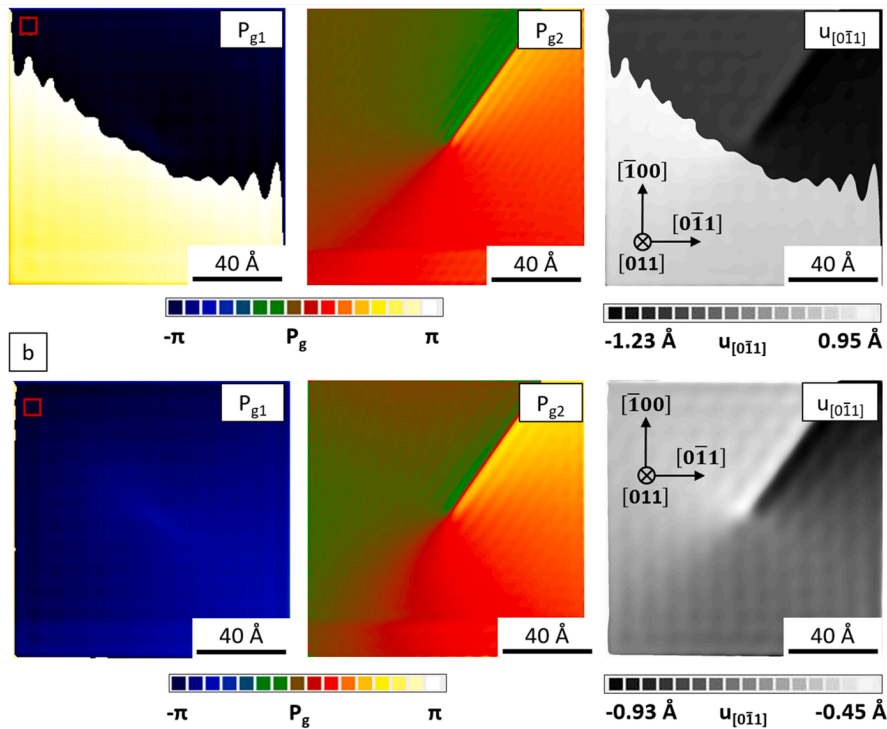


Fig. A5. Influence of  $\pm \pi$  phase transition in GPA on resulting displacement maps for a  $\frac{a}{6}[121]$  dislocation. The images show the phase maps  $P_{g1}$  and  $P_{g2}$  together with the resulting  $[0\bar{1}1]$ -displacements. While the phase shift of  $P_{g1}$  in (a) results to an artifact in  $u_{[0\bar{1}1]}$ , the slightly changed reference area in (b) leads to an even phase distribution and clear perceptibility of the dislocation plane in the displacement map.

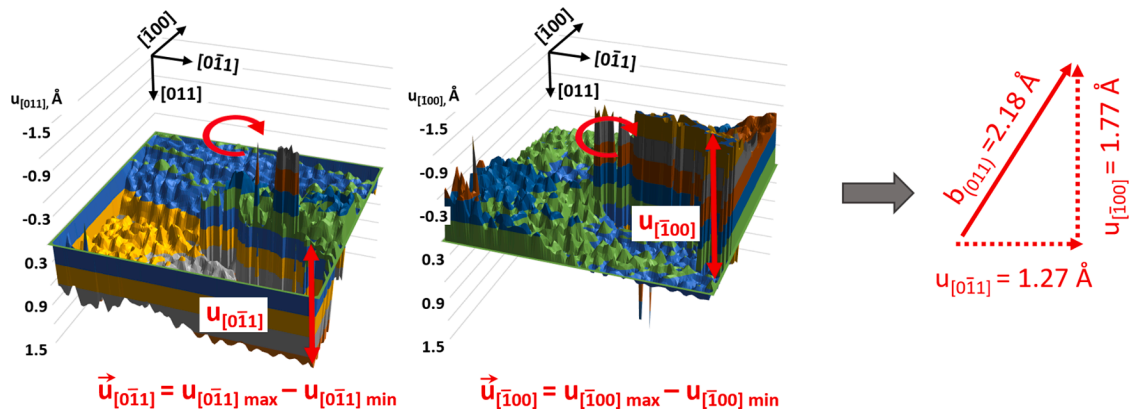


Fig. A6. Burgers vector projection in the (011)plane as obtained by GPA-analysis of the experimental STEM-image shown in Fig. 2(a).

Table A1

Comparison of Burgers vectors calculated from individual projections as obtained by TeMA- and GPA-analysis (cf. Table 2) of the simulated  $\frac{a}{6}[121]$  partial dislocation and the  $\frac{a}{2}[\bar{1}01]$  full dislocation and relative error  $f$  to theoretical vectors given in the bottom row.

	$\frac{a}{6}[121]$ partial dislocation Burgers vector	$f$	$\frac{a}{2}[\bar{1}01]$ full dislocation Burgers vector	$f$
TeMA	$\vec{b} = \begin{pmatrix} 0.81 \\ 1.41 \\ 0.83 \end{pmatrix}$ $ \vec{b}  = 1.83 \text{ \AA}$	4.04° 26.9%	$\vec{b} = \begin{pmatrix} -1.74 \\ -0.04 \\ 1.75 \end{pmatrix}$ $ \vec{b}  = 2.47 \text{ \AA}$	1.00° 1.0%
GPA	$\vec{b} = \begin{pmatrix} 0.62 \\ 1.26 \\ 0.62 \end{pmatrix}$ $ \vec{b}  = 1.53 \text{ \AA}$	0.56° 6.2%	$\vec{b} = \begin{pmatrix} -1.74 \\ -0.03 \\ 1.77 \end{pmatrix}$ $ \vec{b}  = 2.48 \text{ \AA}$	0.80° 0.5%
Theory	$\vec{b} = \begin{pmatrix} 0.59 \\ 1.18 \\ 0.59 \end{pmatrix}$ $ \vec{b}  = 1.44 \text{ \AA}$	- -	$\vec{b} = \begin{pmatrix} -1.76 \\ 0 \\ 1.76 \end{pmatrix}$ $ \vec{b}  = 2.49 \text{ \AA}$	- -

Table A2

Comparison of Burgers vector projections as obtained by TeMA- and GPA-analysis using a reduced atomic lattice.

	$\frac{a}{6}[121]$ partial dislocation		$\frac{a}{2}[\bar{1}01]$ full dislocation		Experiment
	(011) projection	(110) projection	(011) projection	(110) projection	(011) projection
TeMA	$b_{[011]} = 0.69 \text{ \AA}$ $u_{[100]} = -0.40 \text{ \AA}$	$b_{[110]} = 0.72 \text{ \AA}$ $u_{[110]} = -0.44 \text{ \AA}$	$b_{[011]} = 2.05 \text{ \AA}$ $u_{[100]} = -1.65 \text{ \AA}$ $u_{[011]} = 1.23 \text{ \AA}$	$b_{[110]} = 2.10 \text{ \AA}$ $u_{[110]} = 1.20 \text{ \AA}$	$b_{[011]} = 2.08 \text{ \AA}$ $u_{[100]} = -1.63 \text{ \AA}$ $u_{[011]} = 1.29 \text{ \AA}$
GPA	$b_{[011]} = 0.77 \text{ \AA}$ $u_{[100]} = -0.63 \text{ \AA}$ $u_{[011]} = -0.44 \text{ \AA}$	$b_{[110]} = 0.78 \text{ \AA}$ $u_{[110]} = 0.62 \text{ \AA}$ $u_{[110]} = 0.48 \text{ \AA}$	$b_{[011]} = 2.11 \text{ \AA}$ $u_{[100]} = 1.71 \text{ \AA}$ $u_{[011]} = 1.24 \text{ \AA}$	$b_{[110]} = 2.14 \text{ \AA}$ $u_{[110]} = 1.23 \text{ \AA}$	$b_{[011]} = 2.12 \text{ \AA}$ $u_{[100]} = -1.77 \text{ \AA}$ $u_{[011]} = 1.20 \text{ \AA}$

## Appendix B. Nearest neighbor assignment

In Section 5, a limitation of the maximum unambiguously ascertainable displacements was observed, which is ascribable to a nearest neighbor assignment between displaced atoms and reference lattice positions conducted by TeMA. The effects were illustrated for the simple case of unidirectional displacements on a qualitative basis. In the following, a more universal mathematical description applicable to arbitrary displacements is provided. For that, a distinction between the actual displacements and TeMA-generated displacements is made. Such a distinction is possible in case of simulated images because the knowledge of enforced displacement field used to create the deformed lattice is known a priori. These are termed the actual displacements that are sought to be reproduced using advanced atomic-scale displacement-analysis techniques, such as TeMA or GPA.

For the case of 1D displacements the repercussions of the nearest neighbor assignment leading to an abrupt jump in the TeMA-generated displacements are clear. Thus, such a jump occurs when the magnitude of displacement is higher than 50% of the lattice-spacing in the direction of the displacement. Consequently, a neighbor analysis is employed to apply a correction. In extension, if in the analysis of an atomic-resolution HRTEM image (with expected 1D displacements) reveals such an abrupt change in displacements, an argument can be made that such jumps are unphysical. Consequently, a correction in form of a neighbor analysis can be employed in order to reproduce the physical or actual displacement (Eq. (4)).

However, with a 2D atomic-resolution HRTEM image of a deformed lattice, a general 2D displacement profile is expected and sought. For such a case, the manifestations of the nearest-neighbor assignment are not clear and are sensitive to the nature of the actual displacements. For instance, consider the linear displacement profiles used for illustrations in Fig. 5 (rectangular lattice) and Fig. A 3 (hexagonal lattice). At the bottom end of the lattice (at  $y = y_{\max}$ ) in Fig. A 3, no abrupt jump of the  $u_x$ ,  $u_{TeMA}$  displacements is observed, which, in the absence of a priori knowledge of the enforced linear profile, may well be trusted as the actual displacement profile not requiring any correction. Moreover, even if it is known that a correction needs to be applied to  $u_x$ ,  $u_{TeMA}$ , an unambiguous correction as straightforward as provided by the neighbor analysis as given in Eq. (4) cannot be employed to reproduce  $u_{xory, actual}$ .

It is useful to cast the nearest-neighbor assignment in mathematical form. This is done by considering rigid displacements of a hexagonal-lattice, a representative unit cell of which is shown in Fig. B 1(a). This arrangement was chosen deliberately as it corresponds to the projection of the FCC lattice as viewed along the [011] zone-axis, with  $x \parallel [0\bar{1}1]$  and  $y \parallel [100]$  which is equal to the experimental HRTEM image, as shown in Fig. 3. Let the actual rigid displacement be given by the dyad  $\mathbf{u} = (u_x, u_y)$  and the displacement obtained by TeMA be represented as  $\mathbf{u}_{TeMA} = (u_{x-TeMA}, u_{y-TeMA})$ . In the case of 1D displacements (with  $u_y = 0$ ), TeMA can reproduce the actual displacements only if the magnitude of displacement is smaller than 50% of the lattice-spacing (of the projected lattice). This is illustrated in Fig. B 1(b) and (c) and can be cast mathematically in the equation:

$$u_{x-TeMA} = \begin{cases} u_x, & u_x \leq 0.5a_{[0\bar{1}1]} \\ u_x - a_{[0\bar{1}1]}, & u_x > 0.5a_{[0\bar{1}1]} \end{cases} \quad (B1)$$

Note that this equation is exactly opposite to Eq. (4), which is used to correct for the nearest neighbor assignment in Fig. 4. It must be reiterated that in practice, the only data available is  $\mathbf{u}_{TeMA}$  and the objective is to back-track to the actual or physical displacement which generates the deformed lattice. Speaking in terms of the 1D displacement case, the objective is to obtain  $u_x$  from  $u_{x-TeMA}$ . In the 1D case, the need of a correction can be identified by the existence of an unphysical displacement jump in the data. This condition is checked for, and a correction circumventing the nearest-neighbor assignment is applied recovering the actual displacement. Before considering the 2D case, it is prudent to recast the previous equation in a more convenient form:

$$u_{x-TeMA} = \min_{|u|} (u_x, u_x - a_{[0\bar{1}1]}) \quad (B2)$$

For the case of 2D displacements, the scenario is illustrated in Fig. B 1(d) and (e). The displacement of interest is one of the origin atom in the figure. If the displacement is small (Fig. B 1(d)), the displaced site is correctly mapped to the reference atomic site. If the displacement is large (Fig. B 1(e)), then the displaced site can be mapped incorrectly to any one of the neighbors of the original reference atomic site. Both the direction and magnitude of the displacement vector will be incorrect. The nearest-neighbor assignment finds a displacement vector with the least magnitude. This can be

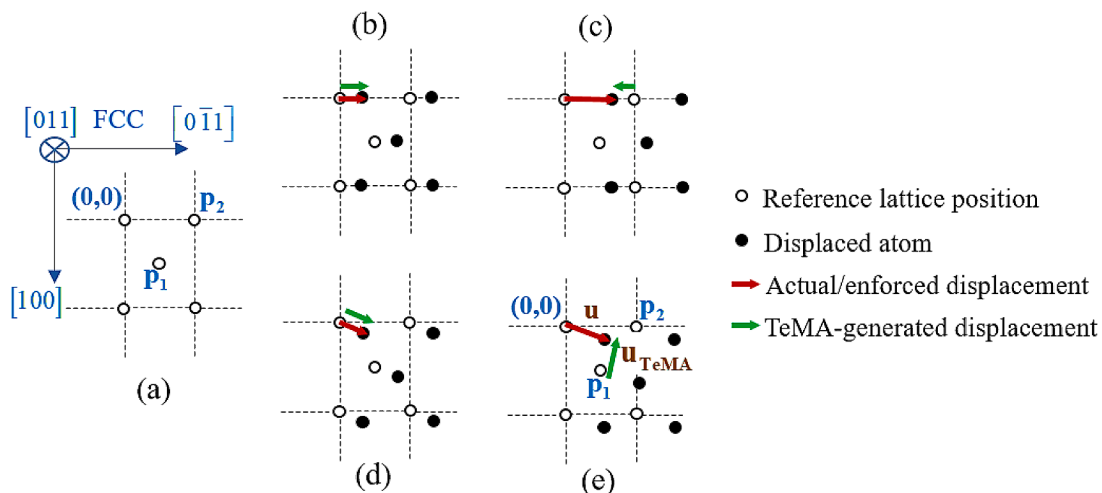


**Fig. B1.** (a) Reference lattice (projection of FCC lattice as seen along the [011] zone axis) with one lattice site marked as the origin (0,0) and two other sites ( $P_1$ ,  $P_2$ ) marked. Small displacements are well-reproduced by TeMA (b and d) whereas largedisplacements lead to erroneous assignment of reference positions and are consequently reproduced incorrectly (c and e). The relation between the TeMA-generated displacement  $\mathbf{u}_{TeMA}$  and the actual displacement  $\mathbf{u}$  is specified by Equation B 3, involving the respective lattice positions  $\mathbf{p}_i$  ( $i = 1, 2, \dots$ ).

expressed analogous to the 1D case as:

$$(u_{x-TeMa}, u_{y-TeMa}) = \min_{|u|}(\mathbf{u}, \mathbf{u} - \mathbf{p}_1, \mathbf{u} - \mathbf{p}_2, \dots) \quad (\text{B3})$$

where  $\mathbf{p}_1 = (0.5a_{[0\bar{1}1]}, 0.5a_{[100]})$ ,  $\mathbf{p}_2 = (a_{[0\bar{1}1]}, 0)$  represent positions of reference lattice sites. The ellipsis indicates that the minimum is sought by comparing the relative position of *all* reference lattice sites that are neighbors to the displaced position.

The question can be asked: What is the maximum displacement that can unambiguously be reproduced by TeMA? The answer is apparent from the previous analysis of 2D displacements. If the displacement vector falls within its Wigner-Seitz cell, the displacements will be correctly reproduced by TeMA. In other words,  $(u_{x-TeMa}, u_{y-TeMa}) = (u_x, u_y)$ . The Wigner-Seitz cell for the chosen lattice is illustrated to the bottom right in Fig. 5. A closed-form limit on the maximum displacement is not trivial to find for the case of general 2D displacements. It is dependent on the direction and the Wigner-Seitz cell, which in turn depends on the lattice constants and zone axis examined.

### Appendix C. Burgers vector projection and displacements across discontinuities

In what follows, the test case of a simulated full dislocation ( $\vec{b} = \frac{a}{2}[\bar{1}01]$ ) is used to show in a first step that the nearest-neighbor assignment performed by TeMA is the reason for the discontinuity line being generated in dependence of different reference lattice origins. In a second step, the reason for why the displacements across this discontinuity nevertheless reflect the magnitude of the Burgers vector is established from a theoretical standpoint. Thus, only analytical data and no results from TeMA are used in this section.

The simulated images for the full  $\vec{b} = \frac{a}{2}[\bar{1}01]$  dislocation were created by enforcing the continuum displacement field solution (derived from the Eshelby-Stroh formalism [58]) on an undeformed reference lattice. In this formalism, the reference origin is at the center of the dislocation. The  $x \parallel [0\bar{1}1]$  component of the displacement field is plotted in Fig. C 1(a). The displacements are offset to reproduce a simple shift of the reference lattice origin to the top left, as shown in Fig. C 1(b). Note that the qualitative distribution as indicated by the gray-scale value is identical and just a different scale bar is used. At this stage, the analytical solution represents the displacements  $\mathbf{u} = (u_x, u_y)$ . The aim is to convert these to the displacements that TeMA is expected to reproduce, i.e.  $\text{TeMA}(\mathbf{u}) = (u_{x-TeMa}, u_{y-TeMa})$ . In order to do that, Equation B 3 is applied and the displacement at each point is modified depending on the stipulated minimizing condition. Consequently, the minimizing condition occurs at a different site and the line indicative of the slip plane in the analytical solution rotates to a different position than what is expected (Fig. C 1(c)). If the reference origin is picked elsewhere (Fig. C 1(d)), the slip plane rotates again (Fig. C 1(e)). As shown in the latter case it may fortuitously align with the expected slip plane but it is only by chance.

Given that the displacements are subject to aberrations (due to the nearest neighbor assignment) that can be as large as 50% of the lattice spacing (shown in Equation B 3), it might be curious that the Burgers vector of the dislocation is rightly reproduced. As this is one of the key conclusions of the present study, a brief argument is provided. The Burgers vector is conventionally obtained by drawing a Burgers circuit around the core of the dislocation [62]. When adapted to the plotted displacement profile, it reduces to estimating the displacement jumps across the line of discontinuity. Hence, the key quantities of interest are  $\Delta u_x = u_{x,B} - u_{x,A} = b_{[0\bar{1}1]} = a/2\sqrt{2}$  and  $\Delta u_y = u_{y,B} - u_{y,A} = b_{[100]} = a/2$  taken across this line (Fig. C 2(a)).

The manifestation of the nearest-neighbor assignment is applied to this solution (cf. Fig. C 2(b)). This is done by combining the enforced displacement field (from linear anisotropic elasticity) with the mathematical form of the nearest neighbor assignment as established in Equation B 3. As elaborated previously, the slip-plane rotates to a different position than what is expected from theory. This occurs because the displacements in the

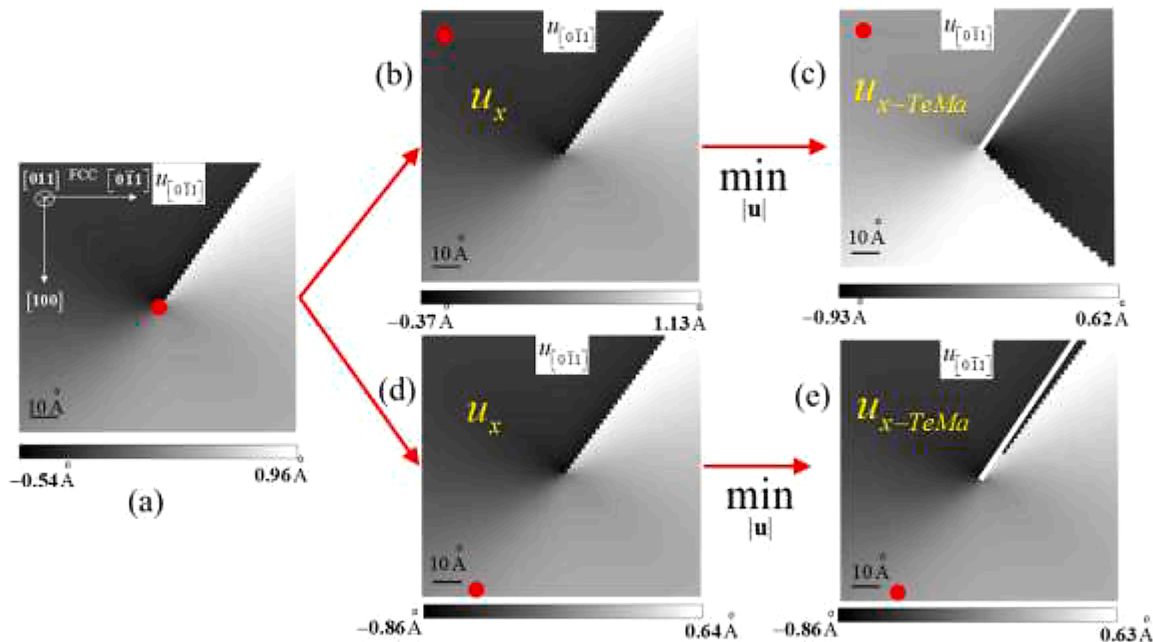


**Fig. C1.** Analytical data showing the rotation of the slip plane due to nearest-neighbor assignment by TeMA. (a)  $[0\bar{1}1]$  component of the analytical solution of displacement fields for the full dislocation. (b and d) Shift of reference origin (red dot) causing an offset in displacements. (c and e) Nearest-neighbor assignment causing a rotation of slip plane (displacement plot that TeMA would reproduce). The white lines represent the actual slip plane known from the analytical solution.

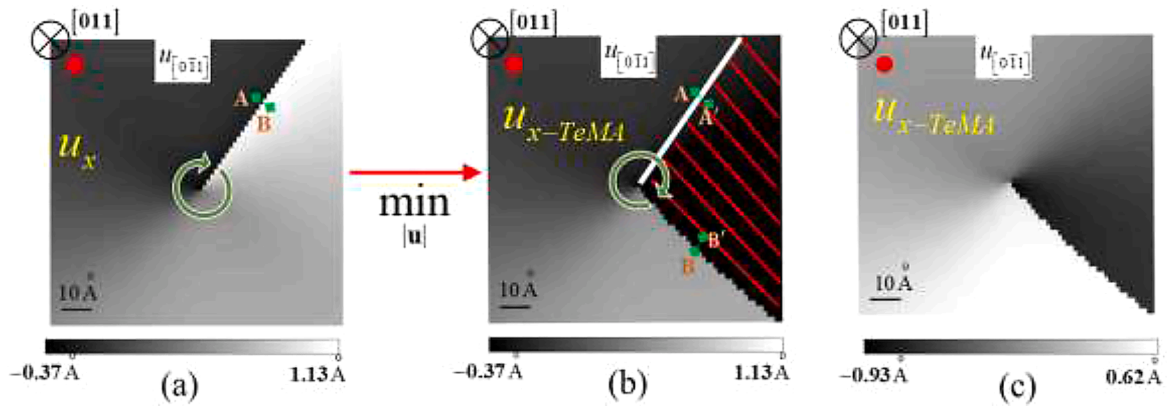


**Fig. C2.** Schematic representation of Burgers vector calculation (here shown for the  $[0\bar{1}1]$  component), with the Burgers circuit represented by the green arrow. The values of displacement across the discontinuity (points labelled with upper case letters) are used for calculation. (a) Burgers circuit drawn on the plot of the analytical solution of the displacement field. (b) Burgers circuit drawn on the displacement plot corrected for nearest-neighbor assignment (TeMA). The hatched area in (b) marks the region of “altered” displacements due to nearest-neighbor assignment (effectively causing a rotation of slip plane). The displacements are plotted with the same scale as in (a). (c) Re-scaled displacement plot after correction by nearest-neighbor assignment (TeMA). The re-scaled plot (same map as Figure A8 (c)) is shown to highlight that the displacement jump across the line of discontinuity is the same as that in the theoretical displacement map in (a) except that this line is rotated to a different orientation.

hatched region change by an amount given by Equation C 1.

$$\mathbf{u}_{TeMa} = (u_{x-TeMa}, u_{y-TeMa}) = \mathbf{u} - \mathbf{p}_3 \quad (C1)$$

where  $\mathbf{p}_3 = (0.5a_{[0\bar{1}1]}, -0.5a_{[100]}) = (a/2\sqrt{2}, -a/2)$ . The displacements are unchanged in the unhatched region, i.e.  $\mathbf{u}_{TeMa} = \mathbf{u}$  there. If the Burgers circuit is drawn in this case, the resulting Burgers vector is given by accounting for two displacement jumps within the circuit. The calculation is shown for the x-component, which is parallel to  $[0\bar{1}1]$ , in Equation C 2.

$$\Delta u_x = (u_{x,B} - u_{x,A}) + (u_{x,B'} - u_{x,A'}) \quad (C2)$$

The discontinuity ( $u_{x,B'} - u_{x,A'}$ ) did not exist before, i.e. in the case of Fig. C 2(a), and was introduced by the nearest-neighbor assignment. This circumstance is given by the x-component of  $\mathbf{p}_3$ . In other words,  $(u_{x,B'} - u_{x,A'}) = a/2\sqrt{2}$ . The jump  $(u_{x,B} - u_{x,A})$  initially represented the x-component of the Burgers vector, but it is diminished by the correction due to the nearest-neighbor assignment and becomes  $(u_{x,B} - u_{x,A}) = b_{[0\bar{1}1]} - a/2\sqrt{2}$ . Summing the displacements at both sites up, the result is the same as before, i.e.

$$\Delta u_x = b_{[0\bar{1}1]} - a/2\sqrt{2} + a/2\sqrt{2} = b_{[0\bar{1}1]} \quad (C3)$$

Also, it is worthwhile to note that, since we are dealing with the full dislocation,  $b_{[0\bar{1}1]} = a/2\sqrt{2}$  and consequently  $(u_{x,B} - u_{x,A}) = 0$ . This is why no displacement jump at the site of the dislocation plane occurred and the plane is not detected, as shown, e.g., in the analytical images (Fig. C 2(c)) and the TeMA images Fig. 6(c). Nevertheless, despite the incapability of TeMA to locate the slip plane for a full dislocation, the Burgers vector calculation carried out in the proposed manner is still reliable and mathematically sound.

## References

- [1] R.W.K. Honeycombe, *The Plastic Deformation in Metals*, 2 ed., Edward Arnold Ltd, Maidenhead, 1984.
- [2] D. Kuhlmann-Wilsdorf, C. Laird, *Dislocation behavior in fatigue*, Mater. Sci. Eng. 27 (1977) 137–156.
- [3] G. Eggeler, et al., Structural and functional fatigue of NiTi shape memory alloys, Mater. Sci. Eng.: A 378 (1–2) (2004) 24–33.
- [4] T. Simon, et al., On the multiplication of dislocations during martensitic transformations in NiTi shape memory alloys, Acta Mater 58 (5) (2010) 1850–1860.
- [5] Y. Bai, et al., Growth of highly tensile-strained Ge on relaxed InGa1-xAs by metal-organic chemical vapor deposition, J. Appl. Phys. 104 (8) (2008), 084518.
- [6] M.L. Lee, et al., Strained Si, SiGe, and Ge channels for high-mobility metal-oxide-semiconductor field-effect transistors, J. Appl. Phys. 97 (1) (2005), 011101.
- [7] R. Peierls, The size of a dislocation, Proceed. Phys. Soc. 52 (1940) 34–37.
- [8] F.R.N. Nabarro, Dislocations in a simple cubic lattice, Proceed. Phys. Soc. 59 (1947) 256–272.
- [9] A.J. Foreman, Factors controlling dislocation widths, Proceed. Phys. Soc. A 64 (1951) 156–163.
- [10] S. Kret, et al., Extracting quantitative information from high resolution microscopy, Phys. Status Solidi 227 (1) (2001) 247–295.
- [11] P. Galindo, et al., High resolution peak measurement and strain mapping using peak pairs analysis, Microsc. Anal. 23 (2) (2009) 23–25.
- [12] F. Hild, S. Roux, Digital image correlation: from displacement measurement to identification of elastic properties - a review, Strain 42 (2006) 69–80.
- [13] T.C. Chu, W.F. Ranson, M.A. Sutton, Applications of digital-image-correlation techniques to experimental mechanics, Exp. Mech. 25 (3) (1985) 232–244.
- [14] F. Ackermann, Digital image correlation: performance and potential application in photogrammetry, Photogramm. Rec. 11 (64) (1984) 423–439.
- [15] N. Floquet, et al., Ferroelectric domain walls in BaTO3: fingerprints in XRPD diagrams and quantitative HRTEM image analysis, J. de Physique III (1997) 1105–1128.
- [16] S. Stemmer, et al., Atomistic structure of 90° domain walls in ferroelectric PbTiO3 thin films, Philosoph. Mag. A 71 (3) (1995) 713–724.
- [17] P.L. Galindo, et al., The peak pairs algorithm for strain mapping from HRTEM images, Ultramicroscopy 107 (12) (2007) 1186–1193.
- [18] R. Bierwolf, et al., Direct measurement of local lattice distortions in strained layer structures by HREM, Ultramicroscopy 49 (1) (1993) 273–285.
- [19] P.H. Jouneau, et al., Strain mapping of ultrathin epitaxial ZnTe and MnTe layers embedded in CdTe, J. Appl. Phys. 75 (11) (1994) 7310–7316.
- [20] M.D. Robertson, et al., Determination of elastic strains in epitaxial layers by HREM, Ultramicroscopy 58 (2) (1995) 175–184.
- [21] S. Kret, et al., Atomic-scale mapping of local lattice distortions in highly strained coherent islands of InGa1-xAs/GaAs by high-resolution electron microscopy and image processing, Philos. Mag. Lett. 77 (5) (1998) 249–256.
- [22] M.J. Hÿtch, Geometric phase analysis of high resolution electron microscope images, Scan. Microsc. 11 (1997) 53–66.
- [23] M.J. Hÿtch, E. Snoeck, R. Kilaas, Quantitative measurement of displacement and strain fields from HREM micrographs, Ultramicroscopy 74 (1998) 131–146.

- [24] M.J. Hÿtch, J.-L. Puteaux, J.-M. Pénisson, Measurement of the displacement field of dislocations to 0.03Å by electron microscopy, *Nature* 423 (6937) (2003) 270–273.
- [25] J.L. Rouvière, E. Sarigiannidou, Theoretical discussions on the geometrical phase analysis, *Ultramicroscopy* 106 (1) (2005) 1–17.
- [26] M.J. Hÿtch, F. Houdellier, Mapping stress and strain in nanostructures by high-resolution transmission electron microscopy, *Microelectron. Eng.* 84 (3) (2007) 460–463.
- [27] D.L. Sales, et al., Critical strain region evaluation of self-assembled semiconductor quantum dots, *Nanotechnology* 18 (47) (2007), 475503.
- [28] J. Kioseoglou, et al., Dislocation core investigation by geometric phase analysis and the dislocation density tensor, *J. Phys. D Appl. Phys.* 41 (3) (2008), 035408.
- [29] V.B. Ozdol, et al., Strain mapping at nanometer resolution using advanced nano-beam electron diffraction, *Appl. Phys. Lett.* 106 (25) (2015), 253107.
- [30] F.I. Allen, et al., High throughput grain mapping with sub-nanometer resolution by 4D-STEM, *Microsc. Microanal.* 25 (S2) (2019) 1960–1961.
- [31] C. Ophus, Four-dimensional scanning transmission electron microscopy (4D-STEM): from scanning nanodiffraction to ptychography and beyond, *Microsc. Microanal.* 25 (3) (2019) 563–582.
- [32] J.-M. Zuo, *Electron Nanodiffraction*, in: P.W. Hawkes, J.C.H. Spence (Eds.), *Springer Handbook of Microscopy*, Springer International Publishing, Cham, 2019, p. 2, 2.
- [33] K. Usuda, et al., Strain relaxation of strained-Si layers on SiGe-on-insulator (SGOI) structures after mesa isolation, *MRS Proceed.* 738 (2002) G13.8.
- [34] K. Müller, et al., Strain measurement in semiconductor heterostructures by scanning transmission electron microscopy, *Microsc. Microanal.* 18 (5) (2012) 995–1009.
- [35] P.F. Rottmann, K.J. Hemker, Nanoscale elastic strain mapping of polycrystalline materials, *Mater. Res. Lett.* 6 (4) (2018) 249–254.
- [36] S.E. Zeltmann, et al., Patterned probes for high precision 4D-STEM bragg measurements, *Ultramicroscopy* 209 (2020), 112890.
- [37] O. Panova, et al., Diffraction imaging of nanocrystalline structures in organic semiconductor molecular thin films, *Nat. Mater.* 18 (8) (2019) 860–865.
- [38] J. Chung, G. Lian, L. Rabenberg, Practical and reproducible mapping of strains in si devices using geometric phase analysis of annular dark-field images from scanning transmission electron microscopy, *IEEE Electron. Device Lett.* 31 (8) (2010) 854–856.
- [39] D. Diercks, et al., Comparison of convergent beam electron diffraction and geometric phase analysis for strain measurement in a strained silicon device, *J. Microsc.* 241 (2) (2011) 195–199.
- [40] M.J. Hÿtch, L. Potez, Gemoetric phase analysis of high-resolution electron microscopy images of antiphase domains: example Cu<sub>3</sub>Au, *Philosoph. Mag. A* 76 (6) (1997) 1119–1138.
- [41] C.W. Zhao, Y.M. Xing, P.C. Bai, Experimental examination of displacement field in an edge dislocation core in aluminum, *Phys. Lett. A* 372 (3) (2008) 312–315.
- [42] Y. Zhu, et al., Interface lattice displacement measurement to 1pm by geometric phase analysis on aberration-corrected HAADF STEM images, *Acta Mater.* 61 (15) (2013) 5646–5663.
- [43] J.-M. Zuo, et al., Lattice and strain analysis of atomic resolution Z-contrast images based on template matching, *Ultramicroscopy* 136 (2014) 50–60.
- [44] P.J. Phillips, et al., Atomic-resolution defect contrast in low angle annular dark-field STEM, *Ultramicroscopy* 116 (2012) 47–55.
- [45] S.J. Pennycook, D.E. Jesson, High-resolution Z-contrast imaging of crystals, *Ultramicroscopy* 37 (1991) 14–38.
- [46] J. Frank, *Three-Dimensional Electron Microscopy of Macromolecular Assemblies: Visualization of Biological Molecules in Their Native State*. Vol. 2, Oxford University Press, New York, 2006.
- [47] S. Kret, et al., Measurement of dislocation core distribution by digital processing of high-resolution transmission electron microscopy micrographs: a new technique for studying defects, *J. Phys.: Condens. Matter* 12 (49) (2000) 10313–10318.
- [48] C.S. Hartley, Y. Mishin, Characterization and visualization of the lattice misfit associated with dislocation cores, *Acta Mater* 53 (5) (2005) 1313–1321.
- [49] T.M. Smith, et al., Atomic-scale characterization and modeling of 60° dislocations in a high-entropy alloy, *Acta Mater.* 110 (2016) 352–363.
- [50] X.D. Xu, et al., Transmission electron microscopy characterization of dislocation structure in a face-centered cubic high-entropy alloy Al<sub>0.1</sub>CoCrFeNi, *Acta Mater.* 144 (2018) 107–115.
- [51] M. Takeda, J. Suzuki, Crystallographic heterodyne phase detection for highly sensitive lattice-distortion measurements, *J. Opt. Soc. Am. A* 13 (7) (1996) 1495–1500.
- [52] H.C. van Assen, M. Egmont-Petersen, J.H. Reiber, Accurate object localization in gray level images using the center of gravity measure: accuracy versus precision, *IEEE Trans. Image Process.* 11 (12) (2002) 1379–1384.
- [53] M. Bönisch, Y. Wu, H. Sehitoglu, Hardening by slip-twin and twin-twin interactions in FeMnNiCoCr, *Acta Mater.* 153 (2018) 391–403.
- [54] Y. Wu, et al., Experimental determination of latent hardening coefficients in FeMnNiCoCr, *Int. J. Plast.* 105 (2018) 239–260.
- [55] A. Stukowski, Visualization and analysis of atomistic simulation data with OVITO—the open visualization tool, *Model. Simul. Mater. Sci. Eng.* 18 (1) (2009), 015012.
- [56] H. Zhang, et al., Elastic properties of Al<sub>x</sub>CrMnFeCoNi (0 ≤ x ≤ 5) high-entropy alloys from ab initio theory, *Acta Mater.* 155 (2018) 12–22.
- [57] K.-H. Kim, Digital micrograph script source listing for a geometric phase analysis, *Appl. Microsc.* 45 (2) (2015) 101–105.
- [58] D.M. Barnett, J. Lothe, An image force theorem for dislocations in anisotropic bicrystals, *J. Phys. F: Metal Phys.* 4 (10) (1974) 1618–1635.
- [59] Z. Wang, et al., Atomic-size and lattice-distortion effects in newly developed high-entropy alloys with multiple principal elements, *Intermetallics* 64 (2015) 63–69.
- [60] L.R. Owen, et al., An assessment of the lattice strain in the CrMnFeCoNi high-entropy alloy, *Acta Mater.* 122 (2017) 11–18.
- [61] L.R. Owen, N.G. Jones, Lattice distortions in high-entropy alloys, *J. Mater. Res.* 33 (19) (2018) 2954–2969.
- [62] J. Weertman, J.R. Weertman, *Elementary Dislocation Theory*, Oxford University Press, 1992.